A New Anisotropic Poroelasticity Model to Describe Damage Accumulation During Cyclic Triaxial Loading of Rock.

Vladimir Lyakhovsky[1], Ivan Panteleev[2], Eyal Shalev[1], John Browning[3, 4], Thomas Mitchell[5], David Healy[6], Philip G. Meredith[5]

[1] *Geological Survey of Israel, Jerusalem, Israel*
[2] *Institute of continuous media mechanics UB RAS, Perm, Russia*
[3] *Pontificia Universidad Catolica de Chile, Santiago, Chile*
[4] *Andean Geothermal Centre of Excellence, Universidad de Chile, Santiago, Chile*
[5] *Department of Earth Sciences, University College London, London, UK*
[6] *School of Geosciences, University of Aberdeen, Aberdeen, UK*

Submitted to Geophys. J. Int.
November 2021
Revised
??? 2022

Abbreviated title: **Anisotropic Poroelastic Damage Model**

Summary

Crustal rocks undergo repeated cycles of stress over time. In complex tectonic environments where stresses may evolve both spatially and temporally, such as volcanoes or active fault zones, these rocks may experience not only cyclic loading and unloading, but also rotation and/or reorientation of stresses. In such situations, any resulting crack distributions form sequentially and may therefore be highly anisotropic. Thus, the tectonic history of the crust as recorded in deformed rocks may include evidence for complex stress paths, encompassing different magnitudes and orientations. Despite this, the ways in which variations in principal stresses influence the evolution of anisotropic crack distributions remain poorly constrained. In this work, we build on the previous non-linear anisotropic damage rheology model by presenting a newly developed poroelastic rheological model which accounts for both coupled anisotropic damage and porosity evolution. The new model shares the main features of previously developed anisotropic damage and scalar poroelastic damage models, including the ability to simulate the entire yield curve through a single formulation. In the new model, the yield condition is defined in terms of invariants of the strain tensor, and so the new formulation operates with directional yield conditions (different values for each principal direction) depending on the damage tensor and triaxial loading conditions. This allows us to discern evolving yield conditions for each principal stress direction and fit the measured amounts of accumulated damage from previous loading cycles. Coupling between anisotropic damage and anisotropic compaction along with the damage-dependent yield condition produces a reasonable fit to the experimentally obtained stress-strain curves. Furthermore, the simulated time-dependent cumulative damage is well correlated with experimentally observed acoustic emissions during cyclic loading in different directions. As such, we are able to recreate many of the features of the experimentally observed directional 3D Kaiser ‘damage memory’ effect.

Keywords: Mechanics, theory, and modelling; Elasticity and anelasticity; Creep and deformation; Fracture and flow.

1. Introduction

It is well-established that crack damage is generated in brittle rocks that are subjected to a level of stress above some crack initiation threshold, and that this cracking results in the output of elastic wave energy in the form of acoustic emissions (AEs) (e.g., Meredith *et al.* 1990, Holcomb 1993, Lockner 1993a). During cyclic loading, cracks close elastically during unloading and re-open elastically during re-loading. If the level of stress during re-loading remains below the peak stress level attained in any previous loading cycle, then no new cracking occurs and no further cracking-related AE is generated. However, on any loading cycle where the previous peak stress is reached or exceed, new cracks are formed and are accompanied by concommittant AE output (Kurita & Fujii 1979, Holcomb & Costin 1986, Li & Nordlund 1993, Lockner 1993a, Pestman & Van Munster 1996, Lavrov 2001, 2003, Browning *et al.* 2017, 2018). This observation of AE output only recommencing when the previous maximum stress level is exceeded is known as the *Kaiser effect* (Kaiser 1953) and is related to the ability of a material to accumulate and reproduce information about previously experienced stress states. However, most experiments that have probed aspects of the Kaiser effect to date have been conducted during either uniaxial or conventional triaxial compression experiments and so have not been able to probe fully for any directionality in crack damage accumulation related to the orientation of principal stresses.

More recently, Browning *et al.* (2017, 2018) investigated the occurrence of a Kaiser effect in samples of Darley Dale sandstone subjected to both conventional and true triaxial stress conditions. Samples were loaded sequentially to increasing levels of peak stress, both with the maximum principal stress maintained in the same orientation and with the maximum principal stress rotated and applied sequentially in three orthogonal orientations. Their results showed that, under true triaxial loading, crack damage is a distinctly directional phenomenon, such that rocks can exhibit a three-dimensional, directionally-dependent Kaiser effect, with AE only being generated when the previous peak stress in any specific orientation was exceeded. They therefore concluded that the Kaiser effect should more accurately be described as a *damage memory effect* rather than a *stress memory effect*.

Traditionally, the analysis of rock deformation and failure criteria has been formulated by, for example, a classical Coulomb-Mohr condition that defines brittle failure, and by a yield cap criterion that defines cataclastic flow (e.g., Issen & Rudnicki 2000). However, these formulations usually ignore any connection between yield stress and the amount of inelastic damage in the form of microcracks, voids, or other flaws that leave the yield stress unchanged, and in doing so, ignore the underlying principle of the Kaiser effect. Laboratory experiments on porous rocks demonstrate evidence of overall strain hardening and yield cap growth attributed to plasticity and porosity loss (Baud *et al.* 2006, Tembe *et al.* 2008, Bedford *et al.* 2018). Several models have been developed for elasto-plastic deformation of isotropic soils, which are commonly formulated in a framework of continuum mechanics and can be successfully applied to model rock behavior with complex yield conditions.

For example, the original Cam-Clay model (Roscoe & Burland 1968) provides a description for the stress versus inelastic strain behavior for yield envelopes of any shape defined in stress space (Muir Wood 1990). Modified Cam-Clay yield functions were successively used in geo-mechanical modelling of hydrocarbon reservoirs (Chan *et al.* 2004, Crawford *et al.* 2011) and in more generic studies of inelastic sandstone deformation (Schultz & Siddharthan 2005, Skurtveit *et al.* 2013). In the modified Cam-clay formulation, the stress conditions required for yield are described by the elliptical function of differential and mean effective stress values. Grueschow & Rudnicki (2005) discussed the various models that incorporate different shapes of the evolving yield caps rather than the elliptic function and compared their model with previous suggested by DiMaggio & Sandler (1971) and Carroll (1991). These studies demonstrated that inelastic behavior of porous rocks are well described by various plasticity models. Pijnenburg *et al.* (2019) quantified the elastic and inelastic contributions to the total deformation behavior of Slochteren sandstones and concluded that not only the expanding yield envelopes, but also change in the elastic moduli should be considered in order to obtain a proper fit to the experimental stress-strain data. Damage rheology models are able to incorporate changes in both the local elastic properties and the form of the porosity-induced yield cap such that deformation patterns and modes of failure can be analyzed alongside the yield cap growth (e.g., Bercovici *et al.* 2001, Stefanov *et al.* 2011, Lyakhovsky *et al.* 2015, Vorobiev 2019).

It has been suggested that the observed Kaiser effect in rocks indicates strain hardening in consecutive cycles such that the phenomena can be attributed to changes in yield surface due to damage accumulation (Holcomb 1993). Damage and yield surface growth are then likely coupled, and constraints on this coupling can aid interpretation of damage localization patterns and the Kaiser effect (Gajst *et al.* 2020). Damage evolution and time-dependent behavior in low porosity sandstones have been investigated (Choens *et al.* 2021) through creep and conventional triaxial experiments, and numerical analyses. Such quasi-static and creep experiments have been successfully simulated using the modified poroelastic damage model of Lyakhovsky *et al.* (2015). As damage accumulates in the samples, the yield cap evolves to keep pace with the strain accumulation.

True triaxial experiments reported by Browning et al. (2017, 2018) demonstrated that the orientation of distributed microcracks in Darley Dale sandstone samples are essentially anisotropic and therefore require an extension of isotropic damage models using a scalar damage parameter and a more complex formulation that introduces a second-order damage tensor (Panteleev *et al.* 2021). The goal of this paper is, therefore, to provide a complete quantitative description of the rheological model with directional yield conditions (i.e., different values for each principal direction) depending on the damage tensor and triaxial loading conditions. The new model combines and extends the results of the previously developed anisotropic damage model of Panteleev *et al.* (2021) and the scalar poroelastic damage model of Lyakhovsky *et al.* (2015). The new analysis includes the ability to simulate yield curves through a single formulation and recreates many of the features of the experimentally observed directionally-dependent Kaiser damage memory effect reported by Browning *et al.* (2018).

2. Anisotropic Poroelastic Damage model

2.1 Damage and porosity

Rock deformation is associated with the formation and growth of internal flaws. From a mechanical point of view, these flaws can be divided into two classes: 1) microcracks (damage) contained in the matrix of a porous rock which act as primary stress raisers or stress concentrators and hence contribute to brittle failure, and 2) pores which can deform and before their collaps act to dissipate or accommodate stress and hence contribute to distributed flow. For an isotropic rock with a sufficiently large number of microcracks and pores, one can define a representative volume in which the flaw density is uniform and described by two scalar variables, damage (α) and porosity (φ). The damage variable is a mechanical variable, which is responsible for the change in material stiffness and brittle failure at a critical level of damage. For anisotropic rocks, we can consider a damage tensor, Ω_{ik}, which represents not only the density of microcracks, but also their orientations. The porosity variable is a geometrical property representing the volume fraction of pores during and after deformation. As an alternative to porosity, we define a compaction-strain tensor, ψ_{ij}, which is equal to the accumulated irreversible strain resulting from loading and unloading. This tensor then represents not only the pore volume change, but also deviations in the shape of the pores.

In the following sub-sections we describe the general thermodynamic approach used to construct the scalar damage and poroelastic damage model, and provide the main equations of the new anisotropic poroelastic damage model. Detailed thermodynamic relations are provided in Appendix A and specific relation for the isotropic and anisotropic model formulations are provided in Appendixes B and C.

2.2 General thermodynamic approach

We derive the main equations of the poroelastic damage model using the basic relations of irreversible thermodynamics, which provide constraints on the rates of dissipative processes (e.g., (Onsager 1931, Biot 1955, Prigogine 1955, Truesdell & Noll 2004, DeGroot & Mazur 2013). This approach has been applied successfully to understand the kinetics of chemical reactions and phase transitions (e.g., Fitts 1962; DeGroot and Mazur 2013), and as the basis for variational methods of continuous media models (e.g., Sedov 1968, 1997, Malvern 1969, Berdichevsky 2009). The constitutive behavior of the material, and flow rules controlling the kinetics of related irreversible processes, is then entirely defined by specification of two potentials. The first is the free energy, F, and the second is the dissipation function or local entropy production, Γ. This approach has been used as the basis for other damage models (e.g. Valanis 1990, Hansen & Schreyer 1994, Lyakhovsky *et al.* 1997, 2015, Bercovici *et al.* 2001, Hamiel *et al.* 2004a,b, Gaede *et al.* 2013). Following Onsager (1931), who theoretically generalized the empirical laws of Fourier, Ohm, Fick, and Navier (see review by Martyushev & Seleznev 2006) , we represent the specific local entropy production as a product of thermodynamic fluxes and thermodynamic forces. For small deviations from equilibrium, the Onsager principle can be obtained from the maximum entropy production principle, the maximum dissipation rate of mechanical energy, or the von Mises principle (e.g., Martyushev & Seleznev 2006, Ziegler 2012). We now discuss the different forms of the energy function, beginning with the scalar isotropic damage formulation, then the coupling isotropic damage and porosity model, and finally we formulate the anisotropic model. The energy and entropy balance equations and general thermodynamic relations are provided in Appendix A.

2.3 Scalar damage and poroelastic damage model

The free energy of a solid (*F*) in the local damage model of Lyakhovsky *et al.* (1997) is assumed to be a function of the state variables, which are the temperature T, the elastic strain tensor $\varepsilon_{ij} = g_{ij}^{(t)} - g_{ij}^{(0)}$ (the difference between the total strain tensor $g_{ij}^{(t)}$ and the irreversible strain tensor $g_{ij}^{(0)}$), and the scalar damage variable α:

$$F = F\left(T, \varepsilon_{ij}, \alpha\right) \qquad (1)$$

Using the balance equations for the energy and entropy, the Gibbs relation and the Murnaghan (1937) definition of the stress tensor, part of local entropy (*Γ*) production associated with evolving damage is:

$$\Gamma = -\frac{\partial F}{\partial \alpha}\frac{d\alpha}{dt} \geq 0 \qquad (2)$$

The complete thermodynamic derivations are presented in the Appendix A, where all the dissipation processes are discussed. Following the Onsager (1931) principle, the kinetic relation for damage evolution is:

$$\frac{d\alpha}{dt} = -C\,\frac{\partial F}{\partial \alpha} \qquad (3)$$

where *C* is the positive kinetic coefficient, which may be either constant or depend on the state variables.

Hamiel *et al.* (2004b) and then Lyakhovsky *et al.* (2015) and extended the scalar damage model to permit coupling of damage and porosity in their formulations. They followed Biot's theory of poroelasticity (Biot 1941, 1956) representing the free energy of a poroelastic medium as a sum of the elastic energy, and the Biot poroelastic coupling terms of the saturated medium. The free energy (1) is extended to be a function of two additional state variables, fluid volume content, ζ, and material porosity, φ:

$$F = F\left(T, \varepsilon_{ij}, \alpha, \varphi, \zeta\right) \qquad (4)$$

As both porosity and damage can evolve with time during deformation, their coupled kinetic equations are derived using a similar balance equation leading to the following local entropy production (Hamiel *et al.* 2004b, Lyakhovsky *et al.* 2015):

$$\Gamma = -\frac{\partial F}{\partial \alpha}\frac{d\alpha}{dt} - \left(\frac{\partial F}{\partial \varphi} + \sigma_m\right)\frac{d\varphi}{dt} \geq 0 \tag{5}$$

where, $\sigma_m = -\sigma_{kk}/3$ is the mean stress. Once more, adopting the relations from Onsager (1931) gives a set of two coupled differential equations (Malvern 1969, DeGroot & Mazur 2013) which define the damage and porosity evolution:

$$\frac{d\varphi}{dt} = -C_{\varphi\varphi}\left(\frac{\partial F}{\partial \varphi} + \sigma_m\right) - C_{\varphi\alpha}\frac{\partial F}{\partial \alpha} \tag{6a}$$

$$\frac{d\alpha}{dt} = -C_{\alpha\varphi}\left(\frac{\partial F}{\partial \varphi} + \sigma_m\right) - C_{\alpha\alpha}\frac{\partial F}{\partial \alpha} \tag{6b}$$

These phenomenological kinetic equations guarantee the non-negative value of entropy production if the matrix of the kinetic coefficients;

$$C_{ij} = \begin{vmatrix} C_{\varphi\varphi} & C_{\varphi\alpha} \\ C_{\alpha\varphi} & C_{\alpha\alpha} \end{vmatrix} \tag{7}$$

meets the following conditions (Malvern 1969, DeGroot & Mazur 2013): the diagonal cells ($C_{\varphi\varphi}$, $C_{\alpha\alpha}$) must be positive, and the off-diagonal terms are usually taken to be either symmetric or antisymmetric. Following the poroelastic damage model of Hamiel *et al.* (2004b) and Lyakhovsky *et al.* (2015) we adopt an antisymmetric structure ($C_{\varphi\alpha} = -C_{\alpha\varphi} = D$) of the kinetic matrix (7). These conditions assure positive dissipation, as in eq. 5. Larger *D*-values then lead to an earlier onset of damage and enhanced accumulation under the same confinement conditions. Hamiel *et al.* (2004b) and Lyakhovsky *et al.* (2015) discussed slightly different forms of the stress- or strain-dependent *D*-value and demonstrated how their scalar poroelastic model reproduces a yield cap and its evolution (see Appendix B for details). Recently Gajst *et al.* (2020) suggested a model with exponential damage-dependent *D*-value:

$$D(\alpha) = D_1 e^{-D_2\alpha}\,(-I_1)^N\sqrt{I_2} \tag{8}$$

where the first coefficient D_1 stands for the initial *D*-value of the damage-free material, and the second coefficient D_2 controls its decrease with increasing damage. The role of the exponent $N>1$ is to control the shape of the yield cap; and this is further discussed in the supplementary materials. Gajst *et al.* (2020) demonstrated that the decrease in the *D*-value with accumulated damage shifts the yield condition or onset of damage to higher stress values and successfully reproduces the Kaiser effect. Since the model is formulated in terms of scalar damage and strain invariants, it accurately reproduces the isotropic Kaiser damage-memory effect, but does not consider the effect of microcrack orientation and stress rotation. The experimentally observed directionally-dependent Kaiser damage-memory effect (Browning *et al.* 2018) hence requires an anisotropic formulation.

2.4 Anisotropic poroelastic damage model

Recently Panteleev *et al.* (2021) extended the scalar isotropic damage model by developing a theoretical model for materials with orthotropic symmetry which describes the material damage using a second rank symmetric tensor, Ω_{ik}, in which the principal directions match the orientation of the principal loading axes. This assumption is supported by results of true triaxial experiments (Browning *et al.* 2017, 2018) which demonstrated that the orientation of distributed microcracks was related to the level and orientation of the principal stresses. Therefore, most of the equations that follow are written with respect to the principal loading directions and stresses, while the complete three-dimensional formulation is presented in Appendix C.

The scalar damage variable α in the free energy form of equation (1) and the poroelastic model with the energy form from equation (4) is substituted by a damage tensor, Ω_{ik}. For the case of an isotropic material ($\Omega_{ij} = \Omega\, \delta_{ij}$), the anisotropic formulation reduces to the scalar model with the damage α equal to a squared value, $\alpha = \Omega^2$. In addition, ~~(~~Lyakhovsky *et al.* (2022)showed that the deformation of pore space is inherently three dimensional and, as such, the compaction-strain strain tensor, ψ_{ij}, should replace porosity in the governing equations. The suggested energy function includes these two tensor state variables; the damage tensor Ω_{ik}, and the compaction-strain tensor ψ_{ij}:

$$F = F\left(T, \varepsilon_{ij}, \Omega_{ij}, \psi_{ij}, \zeta\right) \tag{9}$$

The elastic strain tensor $\varepsilon_{ij} = g_{ij}^{(t)} - \psi_{ij}$ is now defined as a difference between the total strain tensor $g_{ij}^{(t)}$ and the tensor ψ_{ij}. The diagonal part of this tensor, $\varphi = \psi_{ij}\delta_{ij}$ represents the material porosity, while the deviatoric components ($\psi_{ij} - \frac{1}{3}\varphi\, \delta_{ij}$) are associated with anisotropic compaction and other mechanisms related to the irreversible strain accumulation. Using the energy form (9), the dissipation associated with evolving tensors Ω_{ij}, ψ_{ij}, consists of two terms which are proportional to the their rate of change (see Appendix C for detailed derivations):

$$\Gamma = -\frac{\partial F}{\partial \Omega_{ij}}\frac{d\Omega_{ij}}{dt} + \left(\sigma_{ij} - \frac{\partial F}{\partial \psi_{ij}}\right)\frac{d\psi_{ij}}{dt} > 0 \tag{10}$$

The phenomenological kinetic equations share the same structure with the poroelastic formulation (6), but connect the tensor quantities as follows:

$$\frac{d\psi_{ij}}{dt} = C^{\psi\psi}_{ijnm}\left(\sigma_{ij} - \frac{\partial F}{\partial \psi_{ij}}\right) - C^{\psi\Omega}_{ijnm}\frac{\partial F}{\partial \Omega_{ij}} \tag{11a}$$

$$\frac{d\Omega_{nm}}{dt} = C^{\Omega\psi}_{ijnm}\left(\sigma_{ij} - \frac{\partial F}{\partial \psi_{ij}}\right) - C^{\Omega\Omega}_{ijnm}\frac{\partial F}{\partial \Omega_{ij}} \tag{11b}$$

Instead of the matrix (7) of the kinetic coefficients, every matrix term becomes a fourth-rank tensor that can be written as:

$$C_{ijnm} = \begin{vmatrix} C^{\psi\psi}_{ijnm} & C^{\psi\Omega}_{ijnm} \\ C^{\Omega\psi}_{ijnm} & C^{\Omega\Omega}_{ijnm} \end{vmatrix} \tag{12}$$

The kinetic equations (11) guarantee a non-negative value of entropy production if the cells of the matrix of the kinetic coefficients meet conditions like those of the poroelastic model: 1) matrices of the diagonal cells ($C^{\psi\psi}_{ijnm}$, $C^{\Omega\Omega}_{ijnm}$) must be positively defined; and 2) we also adopt an antisymmetric structure ($C^{\Omega\psi}_{ijnm} = -C^{\psi\Omega}_{ijnm}$) for the off-diagonal terms, as was done previously for the poroelastic model.

In the next section, we specify the energy function (9) and kinetic coefficients (12), and then demonstrate the main model features.

2.5 Energy function and kinetic equations, anisotropic model

The energy function for the anisotropic damage model includes a damage tensor Ω_{ij} and so cannot be formulated only in terms of invariants of the strain tensor:

$$\begin{gathered} I_1 = \varepsilon_{ij}\delta_{ij} \\ I_2 = \varepsilon_{ij}\varepsilon_{ij} \end{gathered} \tag{13}$$

Following Murti et al., (1991) and Zhang and Cai, (2010), Panteleev *et al.* (2021) incorporated invariants $I_1^{(\Omega)}$ and $I_2^{(\Omega)}$ of the tensor $\varepsilon_{ij}^{(\Omega)} = \frac{1}{2}\left(\varepsilon_{ik}\Omega_{kj} + \varepsilon_{jk}\Omega_{ki}\right)$. In the coordinate system of the principal damage values, these invariants are (see Appendix C for the general case):

$$\begin{aligned} I_1^{(\Omega)} &= \varepsilon_{11}\Omega_1 + \varepsilon_{22}\Omega_2 + \varepsilon_{33}\Omega_3 \\ I_2^{(\Omega)} &= (\varepsilon_{11}\Omega_1)^2 + (\varepsilon_{22}\Omega_2)^2 + (\varepsilon_{33}\Omega_3)^2 + \\ &\quad + \frac{1}{2}\varepsilon_{12}^2(\Omega_1 + \Omega_2)^2 + \frac{1}{2}\varepsilon_{13}^2(\Omega_1 + \Omega_3)^2 + \frac{1}{2}\varepsilon_{23}^2(\Omega_2 + \Omega_3)^2 \end{aligned} \tag{14}$$

We extend the energy function of Panteleev *et al.* (2021) using additional terms of Biot's theory of poroelasticity (Biot 1941, 1956); see also Hamiel *et al.* (2004b) and Lyakhovsky *et al.* (2015):

$$F = \left[\frac{\lambda_0}{2} I_1^2 + \mu_0 I_2\right] + \left[\mu_1 I_2^{(\Omega)} - \gamma I_1^{(\Omega)} \sqrt{I_2^{(\Omega)}}\right] + \frac{M}{2}\left[\beta I_1 - \zeta + \psi_{ij}\delta_{ij}\right]^2 + Ch\frac{\gamma}{2}\Omega_{ij}\Omega_{ij} \tag{15}$$

The energy function for nonlinear poroelastic damaged media includes two Hookean terms with the Lamé drained moduli of the intact (damage-free) rock λ_0, μ_0 and two second order terms with strain invariants $I_1^{(\Omega)}$ and $I_2^{(\Omega)}$. The modulus μ_1 controls the reduction of the effective shear modulus, and the coupling modulus γ is responsible for enhanced nonlinearity with damage accumulation (Panteleev *et al.* 2021). The third term in squared brackets, with Biot modulus M and coefficient β, differs from the classical poroelasticity only by the term $\psi_{ij}\delta_{ij}$, that represents the porosity. Similarly to the scalar model (Appendix B), we introduce the damage-dependent term with the coefficient *Ch* (Gajst 2020), which allows us to account for the cohesive forces that influence rock fracture under low confining pressures.

Following the definitions of the scalar damage model, we use $\mu_1 = \xi_0\gamma$ with critical ratio $\xi_0 = I_1/\sqrt{I_2}$ of the strain invariants (13). The ξ_0 value is related to the internal friction angle of the intact rock (Agnon & Lyakhovsky 1995) and controls the onset of damage accumulation in the scalar damage model as well as in the anisotropic model for the material with isotropic damage ($\Omega_{ij} = \Omega\,\delta_{ij}$). With this notation, the stress-strain constitutive relation for for *k*-component of the principal stress and damage values is (see Appendix C for complete relation):

$$\sigma_k = \lambda_0 I_1 + 2\mu_0\varepsilon_k - \gamma\Omega_k\sqrt{I_2^{(\Omega)}} + \gamma\left(2\xi_0 - \frac{I_1^{(\Omega)}}{\sqrt{I_2^{(\Omega)}}}\right)\varepsilon_k\Omega_k^2 + \beta M\,(\beta I_1 - \zeta + \psi_k) \tag{16}$$

and the fluid pressure is:

$$p_f = \frac{\partial F}{\partial \zeta} = M\,(-\beta I_1 + \zeta - \psi_n) \tag{17}$$

Similarly to the Biot poroelasticity, the effective stress is defined as:

$$\sigma_{ij}^{eff} = \sigma_{ij} - \frac{\partial F}{\partial \psi_{ij}} \tag{18}$$

Kinetic coefficients (12) should be defined in order to provide the complete form of the kinetic equations (11). The matrix $C^{\Omega\Omega}_{ijnm}$ multiplied by $\partial F/\partial\Omega_{ij}$ defines the damage accumulation rate, driven by the thermodynamic force associated with the damage-dependent energy change. The most conservative assumption to define the components of this matrix is the absence of any interaction between different damage components on their kinetics:

$$C^{\Omega\Omega}_{ijnm} = \frac{L}{\sqrt{\Omega_{ij}\Omega_{ij}}}\left(\delta_{ik}\,\delta_{jn} + \delta_{in}\,\delta_{jk}\right) \tag{19}$$

This form of damage kinetics was verified by Panteleev *et al.* (2021) using results from true triaxial rock mechanics experiments, and is therefore adopted here for the poroelastic model.

The off-diagonal antisymmetric coefficient, noted here as $D_{ijkn} = C^{\Omega\psi}_{ijnm} = -C^{\psi\Omega}_{ijnm}$, controls the coupling between irreversible strain (porosity) and damage accumulation. Extending the Gajst *et al.* (2020) model with an exponential damage-dependent *D*-value (8) to the tensor form and using the same type of strain dependency, we suggest the following form of the coupling kinetic coefficient D_{ijkn}:

$$D_{ijkn} = D_1 exp\left[-D_2\Omega_{ij}\right]\delta_{kn}\,(-I_1)^N\sqrt{I_2} \tag{20}$$

where we use the standard definition of the exponent of the tensor $\boldsymbol{X}_{ij}$ by means of its series representation (Hirsch *et al.* 1974):

$$exp\left(\boldsymbol{X}_{ij}\right) = \sum_{m=0}^{\infty}\frac{\boldsymbol{X}_{ij}^m}{m!} \tag{21}$$

Note that the principal values of the tensor $exp\left(\boldsymbol{X}_{ij}\right)$ are equal to the exponent of the principal value $exp(\boldsymbol{X}_k)$.

Given the kinetic coefficients (19, 20), the equation for the damage evolution (11b) for principal components becomes (see Appendix C for complete relation):

$$\frac{d\Omega_k}{dt} = K\,D_1 exp[-D_2\Omega_k]\,(-I_1)^{N+1}\sqrt{I_2} +$$

$$+\frac{L}{\sqrt{\Omega_l\Omega_l}}\left[\varepsilon_k\sqrt{I_2^{(\Omega)}} + \left(\frac{I_1^{(\Omega)}}{\sqrt{I_2^{(\Omega)}}} - 2\xi_0\right)\varepsilon_k^2\Omega_k - Ch\,\Omega_k\right] \tag{22}$$

The effective mean stress ($\sigma_m^{eff} = -\sigma_{kk}^{eff}/3$) in (11b) was substituted here by the volumetric strain multiplied by the bulk modulus *K* ($\sigma_m^{eff} = -K\,I_1$) leading to the power index *N*+1.

The equation for the irreversible strain accumulation (11a) includes two terms. The first term, $C_{ijnm}^{\psi\psi}\sigma_{nm}^{eff}$, describes compaction/dilation with the rate proportional to the effective stress. The second is the damage-related coupling term multiplied to D_{ijkn} (20), and describes the compaction or dilation associated with the formation and growth of damage. Representing the effective stress as a superposition of the volumetric (σ_m^{eff}) and deviatoric (τ_{ij}) components allows us to describe the different mechanisms of the irreversible strain accumulation, or ψ_{ij} kinetics. The pressure driven compaction in the isotropic case becomes a well-known porosity reduction to its pressure-dependent equilibrium value, or Athy's (1930) law. ~~(~~Lyakhovsky *et al.* (2022)modified the scalar Athy relation and suggested that the 3-D equilibrium compaction depends on both pressure and deviatoric stress components:

$$\psi_{ij}^{(eq)} = B_0\left[\delta_{ij} - exp\left(-\frac{\sigma_m^{eff}}{B_1}\delta_{ij} - \frac{\tau_{ij}}{B_2}\right)\right] \tag{23}$$

which further suggested the kinetics of the pressure-driven 3-D compaction has the form

$$\frac{d\psi_{ij}}{dt} = A\left(\psi_{ij}^{(eq)} - \psi_{ij}\right)\sigma_m^{eff} \tag{24}$$

The equations (23, 24) consider not only the closure of voids or changes in the pore space (isotropic porosity reduction), but also changes in void shape under non-hydrostatic loading. Neglecting the term with deviatoric stress, or taking $B_2 \to \infty$ in (23), reduces both the equilibrium compaction and kinetic equation to the traditional scalar form formulated in terms of material porosity.

Experimental studies suggest that permanent inelastic deformation is not only caused by pressure driven compaction, but also starts to accumulate at the onset of microcracking (as evidenced by the output of AE) and increases all the way up to the point of brittle failure (e.g., Lockner 1993, 1998, Martin & Chandler 1994). This process is usually associated with the growth of microcracks and frictional sliding between grains, rather than closure of voids or space between grains. For similar reasons, Hamiel *et al.* (2004a) related the rate of irreversible strain accumulation with the rate of their scalar damage growth. Keeping in mind that the scalar damage variable is equivalent to the squared damage tensor, we extend their relation to:

$$\frac{d}{dt}\varepsilon_{ij}^{(ir)} = \begin{cases} C_V\frac{d(\Omega_{in}\Omega_{jm})}{dt}\tau_{nm}, & \frac{d(\Omega_{in}\Omega_{jm})}{dt} > 0 \\ 0, & \frac{d(\Omega_{in}\Omega_{jm})}{dt} \leq 0 \end{cases} \tag{25}$$

The final kinetic equation (11) for the ψ_{ij} tensor incorporates all of the discussed mechanisms and to avoid a lengthy expression, is written for principal components:

$$\frac{d\psi_k}{dt} = A\left(\psi_k^{(eq)} - \psi_k\right)\sigma_m^{eff} + C_V\frac{d(\Omega_k^2)}{dt}\tau_k +$$

$$+D_1 exp[-D_2\Omega_k]\,(-I_1)^N\sqrt{I_2}\left[\varepsilon_k\sqrt{I_2^{(\Omega)}} + \left(\frac{I_1^{(\Omega)}}{\sqrt{I_2^{(\Omega)}}} - 2\xi_0\right)\varepsilon_k^2\Omega_k - Ch\,\Omega_k\right] \quad (26)$$

The first term of (26) represents the compaction prior to the onset of damage accumulation, which is a three-dimensional extension of the scalar Athy's compaction law. According to this term, the compaction approaches its stress-dependent equilibrium value with the rate proportional to the effective pressure. The second term is the three-dimensional equivalent of the damage-dependent irreversible strain accumulation with inverse of the effective viscosity or fluidity proportional to the rate of damage accumulation. This term describes extension or compaction depending on the sign of the deviatoric stress component. The last term represents the coupling between damage and porosity kinetics. Its sign, extension or compaction, is defined by the expression in the square brackets and depends on the loading and damage values.

The kinetic expressions for damage (22) and irreversible strain (26) provide the closed system of equations defining the three-dimensional evolution of the material properties.

2.6 Yield cap evolution

The new anisotropic poroelasic damage model shares the main features of the previously developed isotropic model of Lyakhovsky *et al.* (2015), including the ability to simulate the entire yield curve through a single formulation. Their model addressed several different deformation regimes including elastic deformation and pressure-driven compaction, brittle failure, and cataclastic flow. Loading of a rock sample to a level of stress beyond the initial yield surface caused an accumulation of damage and resulted in a porosity change (causing either compaction or dilation). In this case, the modeled yield cap grows. Consequently, if the sample is unloaded and then reloaded, the new yield cap is found to occur at a higher stress state, which is in agreement with the Kaiser effect. These general features of the model yield cap are shown in strain space, i.e., differential strain ($\varepsilon_1 - \varepsilon_3$) versus volumetric strain (Fig.

1) instead more common stress space representation (differ~~t~~ential stress vs. pressure). Several authors formulated yield conditions in terms of strains and demonstrated significant advantages of this approach for materials with evolving yield conditions as a function of material properties and loading history (Naghdi & Trapp 1975, Yoder & Iwan 1981, Han & Chen 1986, Puzrin & Houlsby 2001). Although there are some similarities between stress-space and strain-space formulations, they are not equivalent when material weakening is considered (Casey & Naghdi 1983, Einav 2004, 2005). The yield surface (heavy black line in Fig. 1) represents the onset of the damage accumulation according to kinetic equation (22) reduced to the model version for the isotropic material ($\Omega_{ij} = \Omega\,\delta_{ij}$) and non-cohesive material (*Ch*=0):

$$\frac{d\alpha}{dt} = C_d\left[D_1 e^{-D_2\alpha}(-I_1)^{N+1}\sqrt{I_2} + I_2(\xi - \xi_0)\right] \qquad (27)$$

This form of the damage kinetic equation predicts the onset of damage accumulation ($d\alpha/dt = 0$), or the yield condition expressed in terms of strain invariants:

$$\sqrt{I_2} = [D_1 e^{-D_2\alpha}(-I_1)^N + I_1]/\,\xi_0 \qquad (28)$$

The entire yield curve (heavy black line in Figure 1) is calculated for compactive volumetric strain (I_1) between zero and a certain critical value I_1^*, corresponding to the onset of damage under hydrostatic compaction. The differential strain ($\varepsilon_1 - \varepsilon_3$) were calculated using strain invariants and assuming triaxial loading conditions.The critical value (I_1^*) is defined from the damage onset or yield condition (28) under hydrostatic loading corresponding to the strain invariant ratio $I_1/\sqrt{I_2} = -\sqrt{3}$:

$$I_1^* = -\left(\frac{\sqrt{3}+\xi_0}{\sqrt{3}\cdot D_1 e^{-D_2\alpha}}\right)^{1/N} \qquad (29)$$

The detailed discussion of the size and shape of the yield envelope and the sens~~e~~itivity to the model parameters, including material cohesion, is presented in Appendix B. The red line in Fig. 1 schematically represents the proportional load path with constant strain invariant ratio ($\xi = I_1/\sqrt{I_2} = Const.$). At the initial stage of loading, when the stress level is beneath the yield cap (Regime I), quasi-elastic deformation is accompanied by material strengthening associated with crack closure and compaction (porosity decrease). When the load reaches the yield condition (red star), the damage accumulation starts. Distributed microcracking and grain crushing enable sliding along newly created internal surfaces, collapse of the pore space, and changes in grain packing arrangements leading to an overall porosity decrease. This deformational

Regime II is most prominent under high confining pressures and is usually treated as cataclastic flow associated with compaction. Damage accumulation as well as porosity reduction leads to the decrease of the coupling coefficient *D*, which in the presented version is considered as damage-dependent only (eq. 8). The damage kinetics affects the yield condition (28) and the yield cap evolves as strain is accumulated. This feature allows the Kaiser effect to be reproduced, such that the onset of damage (and its associated AE) occurs at increasingly higher stress levels, if the sample is unloaded and reloaded along the same loading path.

Under elevated values of the differential strain, the loading path crosses the compaction-dilation transition (dashed line in Fig. 1) separating the deformational Regime II with compaction and Regime III with inelastic porosity increase (dilatancy). This transition coincides with the Coulomb-Mohr failure criterion and meets the condition $\xi = \xi_0$. When the loading is pushed beyond the compaction-dilation transition, intensive damage accumulation, along with significant differential strains, lead to material dilation (porosity increase). Damage increase is then bounded by a certain critical value which eventually corresponds with macroscopic brittle failure, a dynamic stress drop, and a rapid conversion of the differential elastic strain into plastic strain components.

The damage kinetic equation (22) of the anisotropic model shares a similar structure to the scalar model (27). It also consists of two competing terms, but their values depend not only on the strain invariants, but also on the direction of loading relative to the principal values of the damage tensor. We re-write these terms assuming that the principal directions of the damage tensor (Ω_k) match the orientation of the principal loading axes with principal strain values ε_k:

$$term_1 = D_1 exp[-D_2\Omega_k]\,(-I_1)^{N+1}\sqrt{I_2} \qquad (30)$$

$$term_2 = \frac{1}{\sqrt{\Omega_l\Omega_l}}\left[\varepsilon_k\sqrt{I_2^{(\Omega)}} + \left(\frac{I_1^{(\Omega)}}{\sqrt{I_2^{(\Omega)}}} - 2\xi_0\right)\varepsilon_k^2\Omega_k - Ch\,\Omega_k\right] \qquad (31)$$

We take out two constants, *K* and *L*, and rescale D_1 to preserve the same proportion between these terms. Figure 2 demonstrates the evolution of these terms and their sums for the conventional loading, where Ω_1 is oriented in the direction of the axial load and ε_1 is the axial strain in the same direction. In this case, Ω_2, Ω_3 are oriented in the direction of the transverse loads with two equal values of strain $\varepsilon_2 = \varepsilon_3$. For the initially isotropic material ($\Omega_1 = \Omega_2 = \Omega_3$), the first term (30) is isotropic, since it depends on the damage and strain invariants. Its value strongly increases with the volumetric deformation (confinement) and weakly depends on the differential strain (Fig. 2a). Values of the second term (31) are however different depending on whether the axial or transverse directions are observed. This is the case even for the isotropic material (Fig. 2 b1 and 2 b2 since the value explicitly depends on the strain components. The axial values (Fig. 2) are always negative and increase (i.e., become more negative) with both volumetric and differential components. Thus, the sum of the first (30) and second (31) terms for the axial direction is negative for most of the strain values except for a small area in the right bottom corner of the map Fig. 2 c1. This implies that damage is not likely to occur in the axial direction. For most of the loading cases, except under high volumetric stress (strain) above critical value, I_1^* (29), the axial damage component remains unchanged or even decreases. Mechanically, this implies that microcracks which are oriented normal to the axial load direction become closed.

The transverse values of the second term (31) are positive at relatively low volumetric strains and elevated differential strains (upper left corner of Fig. 2b1). They become negative with volumetric strain increase. This change is indicated by a heavy red line separating the negative and positive values in Figure 2b2. The summation of the positive and negative values of the first (Fig. 2a) and second (Fig. 2b$_2$) terms forms the yield cap (black heavy line in Fig. 2c2) which separates areas corresponding to damage accumulation (positive values) and healing or microcrack closure (negative values) for the transverse components Ω_2, Ω_3.

The obtained shape of the yield cap for transverse damage components (red line in Fig. 3c2) is very similar to those predicted by the scalar model (see Figs B1-3 in Appendix B). At low volumetric strains (with low level confinement) the yield cap is slightly shifted up depending on the cohesive force values (See Fig B3 in Appendix B for effect of cohesion). Loading above the yield cap leads to gradual accumulation of two transverse damage components, Ω_2, Ω_3, that form at the same rate while the axial damage value, Ω_1, remains unchanged. This situation creates a stress-induced cylindrical transverse damage anisotropy observed in triaxial experiments (Browning *et al.* 2018). The damage can be schematically shown as two families of microcracks (insert in Fig. 3). One family (blue cracks in Fig. 3) is oriented parallel to the axial loading direction and opening in the transverse directions. Another family (black cracks in Fig. 3) normally oriented to the axial loading direction is closed. The axial damage value, Ω_1, remains unchanged until large hydrostatic volumetric strains above certain critical value, I_1^* close to 0.8%, are applied. This value is similar to that predicted by the scalar model (29) and describes the onset of pore space collapse. The anisotropic model predicts that the axial damage increases under the loading conditions in the area on the right of the black dashed line in Fig. 3.

Accumulation of the transverse damage components increases the size of the yield cap which is related to exponential damage-dependence in the first term (30). If the sample is then reloaded, along the same loading path, the damage commences at the point of the previous maximum stress value. This corresponds to the previously mentioned enlargement of the yield cap. This Kaiser effect is schematically shown in Fig. 4 as a “no rotation” cyclic loading. During the first loading cycle (blue path and envelope), the onset of damage occurs at relatively low differential strain (strain values and model parameters will be specified in the next section comparing with experimental results). During the second cycle (purple path and envelope), the onset of damage occurs at a significantly higher value of strain (or stress), close to the maximum level of stress in the previous cycle. The quality of the Kaiser effect then depends on how close the yield cap keeps pace with the strain accumulation. This feature dramatically changes if the loading direction is rotated between consecutive loading cycles. Only a small change between the blue, green, and red yield envelopes is predicted for the case “rotation of the loading direction between cycles”. Similar to the previous case, the starting material has an essentially isotropic distribution of microcracks and flaws at the beginning of the first loading cycle (blue path and envelope in Fig. 4). However, after unloading at the end of the first cycle, the sample is no longer isotropic since new anisotropic microcrack damage has been formed, with the cracks growing parallel to the maximum loading direction (Ω_2, Ω_3) and closure in the plane normal to the maximum loading direction (Ω_1,). For the second loading cycle (red line), the loading orientations are rotated on the same sample that contains the previously formed anisotropic damage, such that the maximum loading direction is parallel to the previous Ω_2,. The low Ω_1 and one of the high Ω_3 damage components are now associated with the transverse direction, while another high component Ω_2 is axial. The onset of accumulation of the new Ω_1 damage component occurs at almost exactly the same level of stress as in the first cycle. There is no observation of any Kaiser effect, and this suggests that a completely new family of microcracks are generated normal to those generated on diring the first cycle. An exactly similar scenario is observed during the third loading cycle when the sample is re-loaded with the loading orientation again rotated such that the $-\Omega_3$ component becomes parallel to the new maximum loading direction (the green path). The onset of damage again occurs at essentially the same level of stress and strain as in cycle 1 and cycle 2. Again, no Kaiser effect is observed. Analysis of Figure 4 explains why there is apparently no Kaiser effect. The blue, red and green lines related to the first, second and third sequential cycles exhibit very similar yield caps which suggests that the new damage on each cycle is independent of the damage formed during earlier cycles. We would therefore not expect to encounter a Kaiser effect under these conditions. It is only when the sample is loaded to a higher level of stress in the same orientation, as demonstrated by the purple line, that would expect to observe a manifestation of the Kaiser effect.

To explain this model prediction further, Figure 5 shows the distribution of damage kinetics terms for the two transverse low Ω_1 and high Ω_3 damage components during the second load cycle for the sample with anisotropic damage $\Omega_1<\Omega_2=\Omega_3$. In spite of the elevated damage in the axial direction, similar to the isotropic sample, the axial damage component, Ω_2, remains unchanged or even decreased or healed (maps are not shown). Values of the first (Fig. 5a1 and a2) and the second (Fig. 5b1 and b2) terms (30, 31) are similar. However, the first term for the Ω_1 component (Fig. 5a2) is slightly larger than for the Ω_3 (Fig. 5a1). The values of the second term show the opposite tendency (Fig. 5b1 and b2). Finally, the sum of these terms controlling the damage kinetics (Fig. 5c1 and c2), gives significantly different yield cap (red heavy lines in Fig. 5 c1,2). Figure 6 summarizes the shape and size of the yield envelope for the anisotropic material (red lines) and compares them with yield caps for the initially isotropic case (dotted lines). The yield cap of the low transverse damage component (red line for Ω_1) is essentially coincident with the yield cap for the isotropic material. However, the yield cap for the high transverse damage component Ω_3 is significantly enlarged. If the loading is not large enough and it is only slightly above the red line for Ω_1 component, the high transverse component Ω_3 remains unchanged and only minor total damage is accumulated in the sample. The yield for the axial Ω_2 component is shifted to significantly higher values of volumetric strain, value, I_1^*

above 1.0%, but retaining the same shape as the yield for the axial component of the isotropic material.

3. Model verification

3.1 Materials and experimental settings

In order to verify the ability of our new model to reproduce the features of the experimentally observed three-dimensional Kaiser effect, we use results from two sets of tests reported by Browning *et al.* (2018), namely; the sequential rotational conventional triaxial (SRCT) loading test, and the cyclic sequential rotational conventional triaxial (CSRCT) loading test. The experiments were conducted on dry samples of the relatively homogeneous Darley Dale sandstone, which is a feldspathic sandstone with a moderate porosity of ~13% and a grain size range from 0.08 to 0.8 mm (Wu *et al.* 2000, Heap *et al.* 2009). The deformation apparatus, based at the laboratories of Koninklijke Shell Exploratie en Produktie Laboratoriu (KSEPL), Rijswijk, Netherlands, consists of a three-axis stressing frame constructed of flanged steel beams, one of which was removable to allow the insertion of the cubic rock samples (edge length of 50 mm). Loading was performed with three pairs of servo-controlled hydraulic rams with a loading capacity of 300 kN. Hemispherical seatings were used along orthogonal axes perpendicular to the faces of the cubic samples and loading platens, with an edge length of 47.5 mm were interposed between the rams and the sample faces to provide the contact surfaces.

In order to keep the sample centered within the apparatus and to ensure good acoustic contact between the sample and the loading platens, a small pre-load of 4 MPa was applied along each of the three axes prior to testing. The load in each of the three directions was measured using electronic load cells with an accuracy of ±0.2%, and the displacement in each direction was measured using linear variable differential transformers (LVDTs) mounted between the loading platens. AE was monitored using a piezo-electric transducer located in a recess within one of the platens.

3.2 Sequential rotational conventional triaxial (SRCT) loading

The SRCT loading test consisted of three loading cycles (Fig. 7a). Prior to the first loading cycle, the sample was pre-loaded hydrostatically up to 4 MPa. Then, in the first loading cycle, the differential stress (blue lines in Figure 7a) was increased in the 1-direction to a maximum value of 80 MPa at a rate of 0.018 MPa/s and then unloaded at the same rate, while both transverse stresses were held constant at 4 MPa. To relate the experimental results to our model formulation, the axial loading direction during the first cycle is associated with the first damage component Ω_1, while the transverse damage components are Ω_2 and Ω_3. In the second cycle, the differential stress was rotated to the 2-direction (red lines in Figure 7a), and the new damage then corresponds to damage component Ω_2, while the transverse components become Ω_1 and Ω_3. The loading protocol was the same as in the first cycle such that the differential load was increased at a rate of 0.018 MPa/s to a maximum value of 80 MPa and then unloaded at the same rate. Again, the two transverse stresses were held constant at 4 MPa. Finally, the same loading protocol was applied in the third cycle following a further rotation of the differential to the 3-direction (green lines in Figure 7a), such that Ω_3 now corresponds to the axial component and Ω_1 and Ω_2 correspond to the transverse components.

Figure 7b (black line) demonstrates that the onset of AE occurs at approximately the same level of stress in each cycle; between 35 and 45 MPa. This suggests that no manifestation of the Kaiser effect is observed in this test. However, while the onset of AE occurs at approximately the same level of stress in each cycle, it is significant to note that the amount of AE (plotted as cumulative AE hits in Figure 7b), decreases with each new sequential loading cycle. The model-simulated accumulated damage curves recreate this tendency for the three loading cycles (colored lines for each cycle in Fig. 7b). The simulation commences with an initially small amount of isotropic damage, $\Omega^2 = \Omega_1^2 + \Omega_2^2 + \Omega_3^2 \approx 1.5\%$. During the first loading cycle, the two transverse damage components, Ω_2 and Ω_3, grow at the same rate (as shown in Fig. 7c) leading to a damage increase, $\Omega^2 \geq 4\%$. However, during the second and third loading cycles, the two transverse damage components (Ω_1 and Ω_3 in cycle 2, Ω_1 and Ω_2 in cycle 3) grow at different rates. This is entirely as expected, because the rock is no longer isotropic following the anisotropic damage formed during the first cycle. The overall amount of damage increase during cycles 2 and 3 together add only slightly more than 1% to the total amount of damage. Finally, the simulated stress-strain curves from the model are shown in Figure 8 (colored lines) and provide a very good fit to the experimental curves (black lines). However, it should be noted that the fitting procedure is done by eye and the search for model parameters is therefore non-unique. There are then several uncertainties and trade-offs between the model parameters. For example, the stresses and strains prior to the onset of damage accumulation (AE output) for the low damage starting material are expected to be linearly elastic, and hence permit the calculation of elastic moduli. However, for this specific test, on a relatively porous sandstone, a significant amount of the total strain is irreversible and associated with material compaction (eq. 23, 24). Panteleev et al., (2021), who processed results for similar experiments on samples of Darley Dale sandstone, also noted this feature. We therefore use Lamé moduli $\lambda_0 = 5\ GPa, \mu_0 = 7\ GPa$ for the starting material. These values are in agreement with the measured seismic wave velocities of V_p ~ 3.4 km/s and V_s ~ 2.1 km/s reported by Browning *et al.* (2017) for this material. Since all tests were performed under the same hydrostatic confining pressure of 4 MPa, it is impossible to constrain the shape of the yield curve. With this uncertainty we use the power index, N=1, in (20); $\xi_0 = -0.1$ and Ch=2 10^{-7} in (22) which corresponds to about 15 MPa of cohesive force (Appendix B). Scaling the range of the damage value, Ω^2, from zero to 100% for total failure (e.g., Lyakhovsky *et al.* 1997) gives $\gamma = 10\ GPa$. Simultaneous fitting of the stresses and strains in the three cycles and the noted similarity between the accumulated damage and the cumulative acoustic emission output led to the following parameters: compaction equilibrium, B_0=0.5%, B_1=20 MPa, B_2=15 MPa in (23), C_v= 3 10^{-2} (MPa s)$^{-1}$ in (25), rate coefficient in (24) A=10^{-5} (MPa s)$^{-1}$, together with L=7 s^{-1}, $K \times D_1$=710^3 s^{-1}, and D_2=30 in (22). The relatively high D_2 value corresponds to the high sensitivity of the yield curve to the change in damage required to reproduce the Kaiser effect (e.g., Gajst *et al.* 2020).

3.3 Cyclic sequential rotational conventional triaxial (CSRCT) loading

CSRCT loading was performed using the same starting material and with the same initial pre-loading of 4 MPa along each of the three sample axes. In the first phase of this test, the differential stress was initially raised to 75 MPa along the 1-direction (i.e., the direction of the Ω_1 damage component) using the same loading rate as for the SRCT test, and the sample was then unloaded instantaneously (Figure 9a). The sample was subsequently reloaded in the same orientation but to a higher differential stress of 80 MPa (blue lines in Fig. 9a), before again being unloaded instantaneously. Then, during the second phase, the differential stress was rotated and applied in the 2-direction (i.e., the direction of the Ω_2 damage component) to a level of 65 MPa in the first cycle and 80 MPa in the second cycle (red lines in Fig. 9a). Finally, in the third phase, the differential stress was rotated again and applied in the 3-direction (i.e., the direction of the Ω_3 damage component). During this phase, the sample was loaded to 55 MPa in the first cycle and 80 MPa in the second cycle (green lines in Fig. 9a). Once again, we see that the model simulated damage curves obtained using the same material properties as for the SRCT test, are very similar in form to the cumulative AE output recorded during the experiment (Fig. 9b). Similarly to the SRCT test, the two transverse damage components, Ω_2 and Ω_3, grow at the same rate (Fig. 9c) during the loading in the 1-direction, as expected for the isotropic sample. However, during the loading in 2- and 3-directions the rock is no longer isotropic following the anisotropic damage formed during the loading in 1-direction. After stress was rotated, the two transverse damage components Ω_1 and Ω_3, and then, after another rotation, components Ω_1 and Ω_2 grow at different rates. The modeled onsets of damage for each loading cycle, are in very good agreement with the measured onsets of AE output for each cycle during the experiment. The colored markers (stars) on the loading curves of Figure 9a indicate the value of stress at the onset of AE, and hence the onset of new damage. We note that both the experimental data and the model simulations exhibit a distinct Kaiser effect when the samples were reloaded in the same direction, but no such effect when the differential stress was rotated. Again, this suggests that the onset of damage is, at best, only weakly affected by damage accumulated during earlier phases when the differential stress was applied in different orientations.

4. Discussion and Concluding Remarks

Here we build on the previous non-linear anisotropic damage rheology model (Panteleev *et al.* 2021) by presenting a newly developed poroelastic rheological model which accounts for both coupled anisotropic damage and porosity evolution. The new model shares the main features of our previously developed anisotropic damage and scalar poroelastic damage models, including the ability to simulate the entire yield curve through a single formulation. In the new model, the yield condition is defined in terms of invariants of the strain tensor, and so the new formulation operates with directional yield conditions (different values for each principal direction) depending on the damage tensor and triaxial loading conditions. This allows us to discern evolving yield conditions for each principal stress direction and fit the measured amounts of accumulated damage from previous loading cycles. Coupling between anisotropic damage and anisotropic compaction along with the damage-dependent yield condition produces a reasonable fit to the experimentally obtained stress-strain curves. Furthermore, the simulated time-dependent cumulative damage is well correlated with experimentally observed acoustic emissions during cyclic loading in different directions. As such, we are able to recreate many of the features of the experimentally observed directional 3D Kaiser 'damage memory' effect.

The main finding from this formulation is that each independent direction will posses its own yield envelope. The state of each envelope then depends on the direction, magnitude and history of loading. Yield in the transverse components are similar in shape but not necessarily in value to the conventional scalar criterion and the yield criterion in the axial direction has an entirely different shape. As such, damage accumulation in the axial direction is possible only under high volumetric stresses.

These results are important in nature since rocks in complex tectonic environments, such as volcanoes or active fault zones, experience stresses that evolve both spatially and temporally and experience not only cyclic loading and unloading, but also rotation and/or reorientation of stresses. The resulting crack natural distributions will then form sequentially and may be highly anisotropic. Thus, the tectonic history of the crust as recorded in deformed rocks may include evidence for complex stress paths, encompassing different magnitudes and orientations. Geodetic and seismic data from periods of inflation and deflation at Krafla volcano in Iceland demonstrates that the rate of seismicity increases only after the amount of inflation in a previous cycle has been reached or exceeded (Heimisson *et al.* 2015). These, and similar observations, point to a potential crustal scale Kaiser effect but the directionality of fracture populations formed has received less attention. The data from Heimisson *et al.* (2015) were interpreted assuming a conventional Kaiser effect such that the orientation ofloading and unloading of all of the episodes were assumed to stress the crustal rocks in the same direction. It is noted that, prior to many cyclic inflation episodes at active volcanoes, the level of inflation has often been at a higher level the than the first cycle of a new episode. In such circumstances, the first cycle should not produce seismicity, as the previous level of inflation has not been reached or exceeded. This has traditionally been explained as related to crack healing processes between cycles (Kim *et al.* 2014) but it can also be explained by our new three-dimensional model. As the orientation and magnitude of crustal stresses can vary enormously between different rock layers (Gudmundsson 2011) the new inflation episode may have loaded the rocks under a slightly different axis and hence triggered seismicity at lower stresses, similar to as demonstrated in Figure 9a.

Recent experimental results have shown that damage, under true triaxial loading, is a distinctly directional phenomenon, and these results have also revealed a 3D directionally dependent Kaiser 'damage memory' effect. The developments of this study provide an internally consistent framework for simulating evolving crustal rock damage under repeated cycles of stress in complex tectonic environments where stresses may evolve both spatially and temporally.

Acknowledgments

The paper benefited from useful comments by two referees, Manolis Veveakis and Klaus Regenauer-Lieb, and the editor, Alexis Maineult. The contributions by Lyakhovsky and Shalev was supported by grant from the Israel Science Foundation, ISF 363/20. The contributions by Browning, Meredith, Healy and Mitchell were supported by UKRI NERC awards NE/N003063/1, NE/N002938/1, NE/T007826/1, NE/T00780X/1. The contributions by Browning was also supported by FONDECYT grant number 11190143. The contribution by Panteleev was supported by Russian Science Foundation (project N 19-77-30008).

Data Availability

Experimental data may be obtained from J.B. (e-mail: jbrowning@ing.puc.cl).

References

Agnon, A. & Lyakhovsky, V. (1995) *Damage distribution and localization during dyke intrusion*. (G. Baer & A. Heimann, Eds.), Rotterdam: Balkema.

Athy, L.F. (1930) Density, porosity, and compaction of sedimentary rocks. *Am. Assoc. Pet. Geol. Bull.*, **14**, 1–24. doi:10.1306/3D93289E-16B1-11D7-8645000102C1865D

Baud, P., Vajdova, V. & Wong, T. -f. (2006) Shear-enhanced compaction and strain localization: Inelastic deformation and constitutive modeling of four porous sandstones. *J. Geophys. Res. Solid Earth*, **111**. doi:doi.org/10.1029/2005JB004101

Bedford, J.D., Faulkner, D.R., Leclère, H. & Wheeler, J. (2018) High-resolution mapping of yield curve shape and evolution for porous rock: The effect of inelastic compaction on porous bassanite. *J. Geophys. Res. Solid Earth*, **123**, 1217–1234.

Bercovici, D., Ricard, Y. & Schubert, G. (2001) A two-phase model for compaction and damage: 1. General theory. *J. Geophys. Res. Solid Earth*, **106**, 8887–8906.

Berdichevsky, V.L. (2009) Variational principles. in *Variational Principles of Continuum Mechanics*, pp. 3–44, Springer.

Biot, M.A. (1941) General theory of three-dimensional consolidation. *J. Appl. Phys.*, **12**, 155–164.

Biot, M.A. (1955) Variational principles in irreversible thermodynamics with application to viscoelasticity. *Phys. Rev.*, **97**, 1463.

Biot, M.A. (1956) General solutions of the equations of elasticity and consolidation for a porous material. *J. appl. Mech*, **23**, 91–96.

Browning, J., Meredith, P.G., Stuart, C., Harland, S., Healy, D. & Mitchell, T.M. (2018) A directional crack damage memory effect in sandstone under true triaxial loading. *Geophys. Res. Lett.*, **45**, 6878–6886.

Browning, J., Meredith, P.G., Stuart, C.E., Healy, D., Harland, S. & Mitchell, T.M. (2017) Acoustic characterization of crack damage evolution in sandstone deformed under conventional and true triaxial loading. *J. Geophys. Res. Solid Earth*, **122**, 4395–4412. doi:10.1002/2016JB013646

Carroll, M.M. (1991) A critical state plasticity theory for porous reservoir rock. *Recent Adv. Mech. Struct. Contin.*, **117**, 1–8.

Casey, J. & Naghdi, P.M. (1983) On the nonequivalence of the stress space and strain space formulations of plasticity theory.

Chan, A.W., Hagin, P.N. & Zoback, M.D. (2004) Viscoplastic deformation in unconsolidated reservoir sands: Field applications using dynamic DARS analysis. *ARMA/NARMS*.

Choens, R.C., Bauer, S.J., Shalev, E. & Lyakhovsky, V. (2021) Modelling yield cap evolution in sandstone based on brittle creep experiments. *Int. J. Rock Mech.*

Min. Sci., **141**, 104706. doi:doi.org/10.1016/j.ijrmms.2021.104706

Coussy, O. (1995) *Mechanics of porous continua*, Wiley.

Coussy, O., Dormieux, L. & Detournay, E. (1998) From mixture theory to Biot's approach for porous media. *Int. J. Solids Struct.*, **35**, 4619–4635, Elsevier.

Crawford, B.R., Sanz, P.F., Alramahi, B. & DeDontney, N.L. (2011) Modeling and prediction of formation compressibility and compactive pore collapse in siliciclastic reservoir rocks. *45th US Rock Mech. Symp.*, OnePetro.

DeGroot, S.R. & Mazur, P. (2013) *Non-equilibrium thermodynamics*, Amsterdam: NorthHolland Publishing Co.

Detournay, E. & Cheng, A. (1993) Fundamentals of poroelasticity. in *Analysis and design methods*, pp. 113–171, Elsevier.

DiMaggio, F.L. & Sandler, I.S. (1971) Material model for granular soils. *J. Eng. Mech. Div.*, **97**, 935–950, American Society of Civil Engineers.

Einav, I. (2004) Thermomechanical relations between stress-space and strain-space models. *Geotechnique*, **54**, 315–318.

Einav, I. (2005) Energy and variational principles for piles in dissipative soil. *Geotechnique*, **55**, 515–525.

Fitts, D.D. (1962) *Nonequilibrium thermodynamics*, New York: McGraw-Hill.

Gaede, O., Karrech, A. & Regenauer-Lieb, K. (2013) Anisotropic damage mechanics as a novel approach to improve pre- and post-failure borehole stability analysis. *Geophys. J. Int.*, **193**, 1095–1109. doi:10.1093/gji/ggt045

Gajst, H. (2020) *Deformation Bands, Damage Localization Processes and Damage Rheology*, PhD. thesis, Tel-Aviv, Israel.

Gajst, H., Shalev, E., Weinberger, R., Marco, S., Zhu, W. & Lyakhovsky, V. (2020) Relating strain localization and Kaiser effect to yield surface evolution in brittle rocks. *Geophys. J. Int.*, **221**, 2091–2103. doi:10.1093/gji/ggaa130

Gibbs, J.W. (1961) *Scientific Papers: Thermodynamics*, Vol. 1, Dover Publications.

Grueschow, E. & Rudnicki, J.W. (2005) Elliptic yield cap constitutive modeling for high porosity sandstone. *Int. J. Solids Struct.*, **42**, 4574–4587.

Gudmundsson, A. (2011) *Rock fractures in geological processes*, Cambridge University Press.

Hamiel, Y., Liu, Y., Lyakhovsky, V., Ben-Zion, Y. & Lockner, D. (2004) A viscoelastic damage model with applications to stable and unstable fracturing. *Geophys. J. Int.* doi:10.1111/j.1365-246X.2004.02452.x

Hamiel, Y., Lyakhovsky, V. & Agnon, A. (2004) Coupled evolution of damage and porosity in poroelastic media: Theory and applications to deformation of porous rocks. *Geophys. J. Int.* doi:10.1111/j.1365-246X.2004.02172.x

Han, D.J. & Chen, W.-F. (1986) Strain-space plasticity formulation for hardening-softening materials with elastoplastic coupling. *Int. J. Solids Struct.*, **22**, 935–950.

Hansen, N.R. & Schreyer, H.L. (1994) A thermodynamically consistent framework for theories of elastoplasticity coupled with damage. *Int. J. Solids Struct.*, **31**, 359–389.

Heap, M.J., Baud, P., Meredith, P.G., Bell, A.F. & Main, I.G. (2009) Time-dependent brittle creep in Darley Dale sandstone. *J. Geophys. Res. Solid Earth*, **114**.

Heimisson, E.R., Einarsson, P., Sigmundsson, F. & Brandsdóttir, B. (2015) Kilometer-scale Kaiser effect identified in Krafla volcano, Iceland. *Geophys. Res. Lett.*, **42**, 7958–7965.

Hirsch, M.W., Devaney, R.L. & Smale, S. (1974) *Differential equations, dynamical systems, and linear algebra*, Vol. 60, Academic press.

Holcomb, D.J. (1993) General theory of the Kaiser effect. *Int. J. Rock Mech. Min. Sci. Geomech. Abstr.*, Vol. 30, pp. 929–935.

Holcomb, D.J. & Costin, L.S. (1986) Detecting damage surfaces in brittle materials using acoustic emissions. *J. Appl. Mech.*, **53**, 536.

Issen, K.A. & Rudnicki, J.W. (2000) Conditions for compaction bands in porous rock. *J. Geophys. Res. Solid Earth*, **105**, 21529–21536.

Kaiser, J. (1953) Erkenntnisse und Folgerungen aus der Messung von Geräuschen bei Zugbeanspruchung von metallischen Werkstoffen. *Arch. für das Eisenhüttenwes.*, **24**, 43–45.

Kim, K., Kemeny, J. & Nickerson, M. (2014) Effect of rapid thermal cooling on mechanical rock properties. *Rock Mech. rock Eng.*, **47**, 2005–2019.

Kurita, K. & Fujii, N. (1979) Stress memory of crystalline rocks in acoustic emission. *Geophys. Res. Lett.*, **6**, 9–12.

Lavrov, A. (2001) Kaiser effect observation in brittle rock cyclically loaded with different loading rates. *Mech. Mater.*, **33**, 669–677.

Lavrov, A. (2003) The Kaiser effect in rocks: principles and stress estimation techniques. *Int. J. Rock Mech. Min. Sci.*, **40**, 151–171.

Li, C. & Nordlund, E. (1993) Experimental verification of the Kaiser effect in rocks.

Rock Mech. Rock Eng., **26**, 333–351.

Lockner, D.A. (1993) The role of acoustic emission in the study of rock fracture. *Int. J. Rock Mech. Min. Sci. Geomech. Abstr.*, Vol. 30, pp. 883–899.

Lockner, D.A. (1993) Room temperature creep in saturated granite. *J. Geophys. Res. Solid Earth*, **98**, 475–487.

Lockner, D.A. (1998) A generalized law for brittle deformation of Westerly granite. *J. Geophys. Res. Solid Earth*, **103**, 5107–5123. doi:10.1029/97JB03211

Lyakhovsky, V., Ben-Zion, Y. & Agnon, A. (1997) Distributed damage, faulting, and friction. *J. Geophys. Res. Solid Earth*, **102**, 27635–27649. doi:10.1029/97jb01896

Lyakhovsky, V., Shalev, E., Panteleev, I. & Mubassarova, V. (2022) Compaction, strain, and stress anisotropy in porous rocks. *Geomech. Geophys. Geo-Energy Geo-Resources*, **8**. doi.org/10.1007/s40948-021-00323-9

Lyakhovsky, V., Zhu, W. & Shalev, E. (2015) Visco-poroelastic damage model for brittle-ductile failure of porous rocks. *J. Geophys. Res. Solid Earth*, **120**. doi:10.1002/2014JB011805

Malvern, L.E. (1969) Introduction to the Mechanics of a Continuous Medium, Pretence Hall Inc. *Englewood Cliffs New jersey*.

Martin, C.D. & Chandler, N.A. (1994) The progressive fracture of Lac du Bonnet granite. *Int. J. Rock Mech. Min. Sci.*, **31**, 643–659, Pergamon. doi:10.1016/0148-9062(94)90005-1

Martyushev, L.M. & Seleznev, V.D. (2006) Maximum entropy production principle in physics, chemistry and biology. *Phys. Rep.*, **426**, 1–45.

Meredith, P.G., Main, I.G. & Jones, C. (1990) Temporal variations in seismicity during quasi-static and dynamic rock failure. *Tectonophysics*, **175**, 249–268.

Muir Wood, D. (1990) *Soil behaviour and critical state soil mechanics*, Cambridge university press.

Murnaghan, F.D. (1937) Finite deformations of an elastic solid. *Am. J. Math.*, **59**, 235–260.

Murti, V., Zhang, W. & Valliappan, S. (1991) Stress invariants in an orthotropic damage space. *Eng. Fract. Mech.*, **40**, 985–990. doi:doi.org/10.1016/0013-7944(91)90164-V

Naghdi, P.M. & Trapp, J.A. (1975) The significance of formulating plasticity theory with reference to loading surfaces in strain space. *Int. J. Eng. Sci.*, **13**, 785–797.

Onsager, L. (1931) Reciprocal relations in irreversible processes. I. *Phys. Rev.*, **37**, 405.

Panteleev, I., Lyakhovsky, V., Browning, J., Meredith, P.G., Healy, D. & Mitchell, T.M. (2021) Non-linear anisotropic damage rheology model: theory and experimental verification. *Eur. J. Mech.*, **85**, 104085.

Pestman, B.J. & Munster, J.G. Van. (1996) An acoustic emission study of damage development and stress-memory effects in sandstone. *Int. J. rock Mech. Min. Sci. Geomech. Abstr.*, Vol. 33, pp. 585–593.

Pijnenburg, R.P.J., Verberne, B.A., Hangx, S.J.T. & Spiers, C.J. (2019) Inelastic Deformation of the Slochteren Sandstone: Stress-Strain Relations and Implications for Induced Seismicity in the Groningen Gas Field. *J. Geophys. Res. Solid Earth*, **124**, 5254–5282. doi:doi.org/10.1029/2019JB017366

Prigogine, I. (1955) Introduction to thermodynamics of irreversible processesles, Springfield, Illinois: Academic Press.

Puzrin, A.M. & Houlsby, G.T. (2001) Fundamentals of kinematic hardening hyperplasticity. *Int. J. Solids Struct.*, **38**, 3771–3794.

Roscoe, K.H. & Burland, J.B. (1968) On the generalized stress-strain behaviour of wet clay. in *Engineering Plasticity* eds. Hayman, J. & Lockhead, F.A., pp. 535–409, Cambridge University Press.

Schultz, R.A. & Siddharthan, R. (2005) A general framework for the occurrence and faulting of deformation bands in porous granular rocks. *Tectonophysics*, **411**, 1–18.

Sedov, L.I. (1968) Variational methods of constructing models of continuous media. in *Irreversible aspects of continuum mechanics and transfer of physical characteristics in moving fluids*, pp. 346–358, Springer.

Sedov, L.I. (1997) *Mechanics of continuous media*, World Scientific.

Skurtveit, E., Torabi, A., Gabrielsen, R.H. & Zoback, M.D. (2013) Experimental investigation of deformation mechanisms during shear-enhanced compaction in poorly lithified sandstone and sand. *J. Geophys. Res. Solid Earth*, **118**, 4083–4100.

Stefanov, Y.P., Chertov, M.A., Aidagulov, G.R. & Myasnikov, A.V. (2011) Dynamics of inelastic deformation of porous rocks and formation of localized compaction zones studied by numerical modeling. *J. Mech. Phys. Solids*, **59**, 2323–2340. doi:doi.org/10.1016/j.jmps.2011.08.002

Tembe, S., Baud, P. & Wong, T. -f. (2008) Stress conditions for the propagation of discrete compaction bands in porous sandstone. *J. Geophys. Res. Solid Earth*, **113**.

Truesdell, C. & Noll, W. (2004) The non-linear field theories of mechanics. in *The non-linear field theories of mechanics*, pp. 1–579, Springer.

Valanis, K.C. (1990) A theory of damage in brittle materials. *Eng. Fract. Mech.*, **36**, 403–416. doi:10.1016/0013-7944(90)90288-R

Vorobiev, O.Y. (2019) Geodyn Material Library: Pseudocap models for dry porous rocks, LLNL-TR-637532.

Wu, X.Y., Baud, P. & Wong, T.-F. (2000) Micromechanics of compressive failure and spatial evolution of anisotropic damage in Darley Dale sandstone. *Int. J. Rock Mech. Min. Sci.*, **37**, 143–160.

Yoder, P.J. & Iwan, W.D. (1981) On the formulation of strain-space plasticity with multiple loading surfaces. *J. Appl. Mech.*, **48**, 773–778.

Zhang, W. & Cai, Y. (2010) *Continuum damage mechanics and numerical applications*, Springer Science & Business Media.

Ziegler, H. (2012) *An introduction to thermomechanics*, Elsevier.

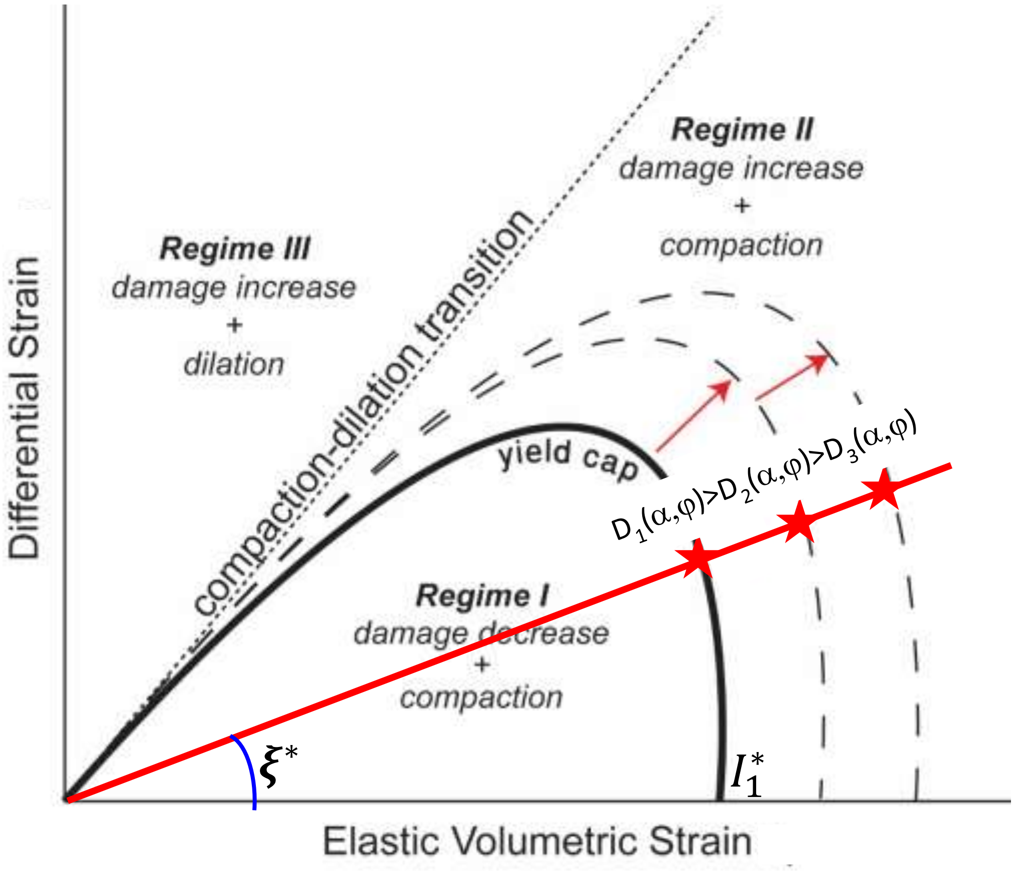

Fig. 1. Three different deformational regimes and growing yield surface neglecting the cohesive force

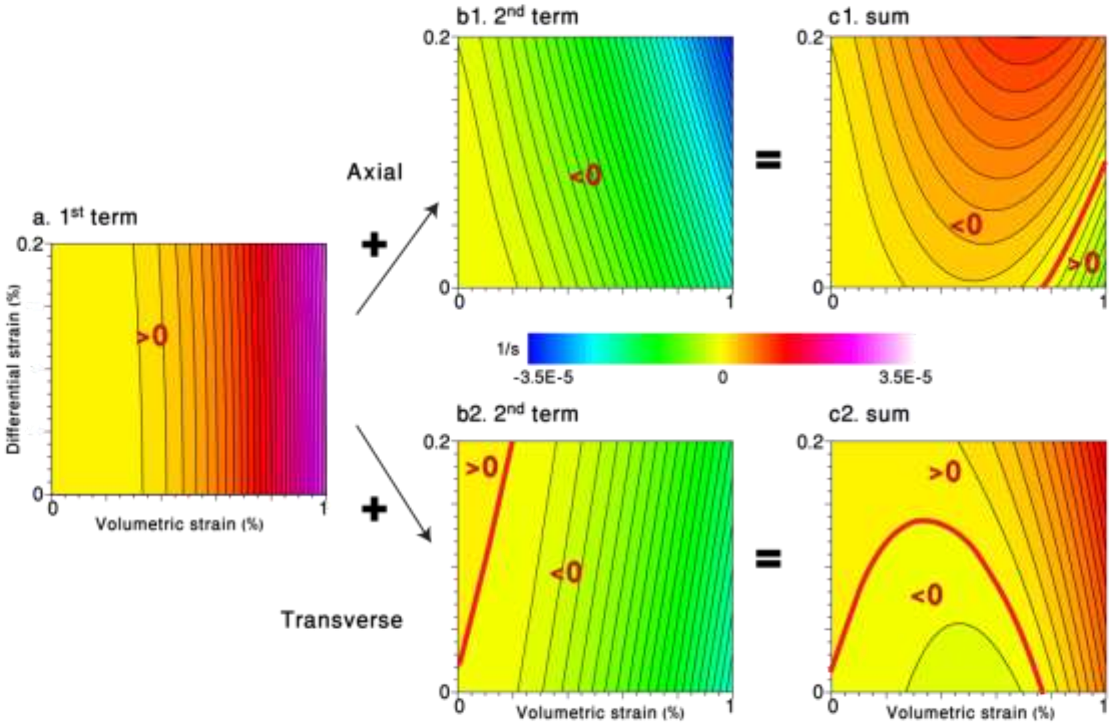

Fig. 2 Damage kinetics for initially isotropic damage ($\Omega_1 = \Omega_2 = \Omega_3$) under conventional triaxial loading. (a) The 1st term is the same for all damage components. The 2nd term for axial component (b1) significantly differs from the values for the transversal components (b2). The damage kinetics in the axial direction (c1) differs from the transversal components(c2) which is similar in shape but not necessarily in values to the conventional scalar criterion.

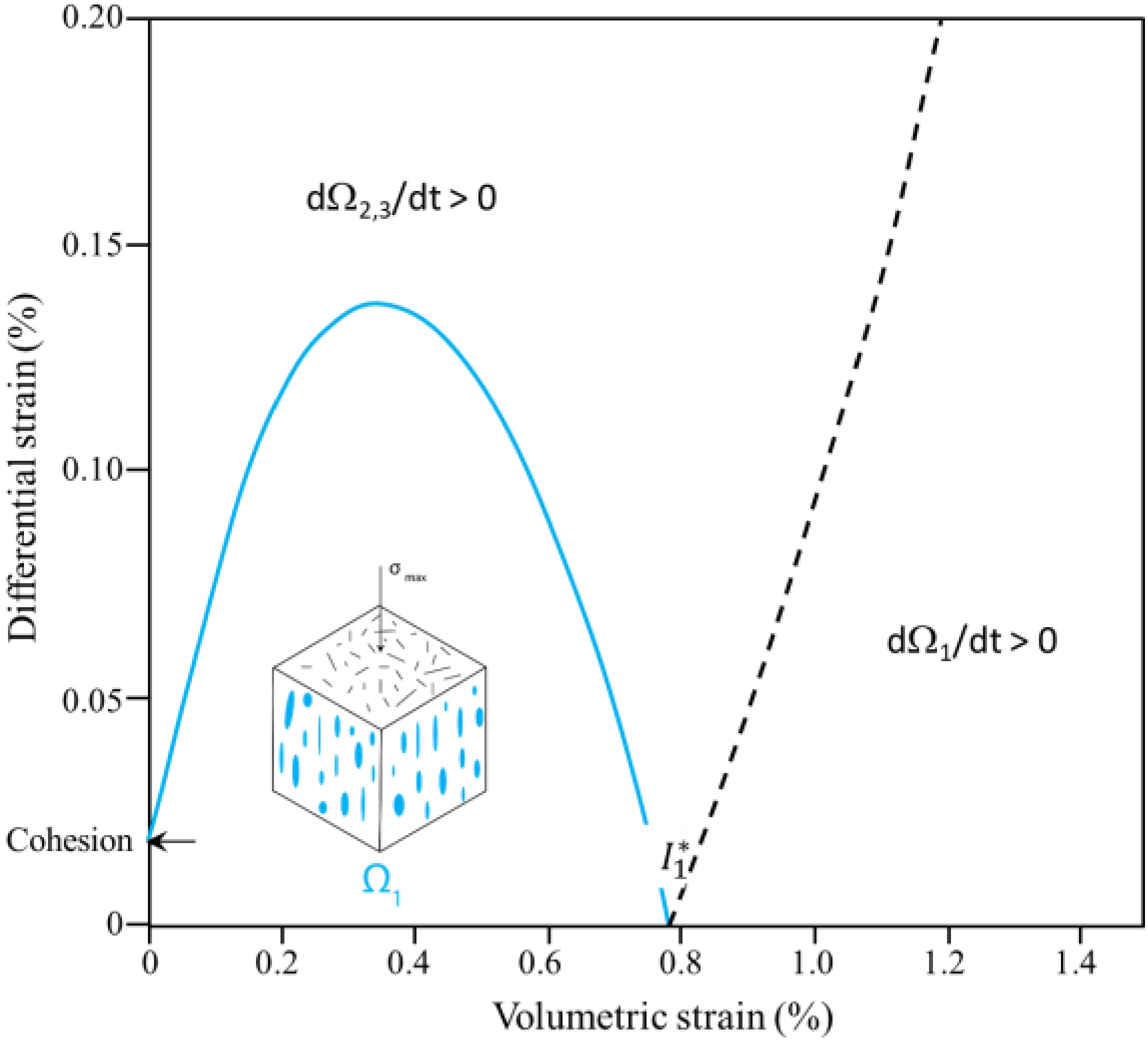

Fig. 3. Yield envelope for initially isotropic material.

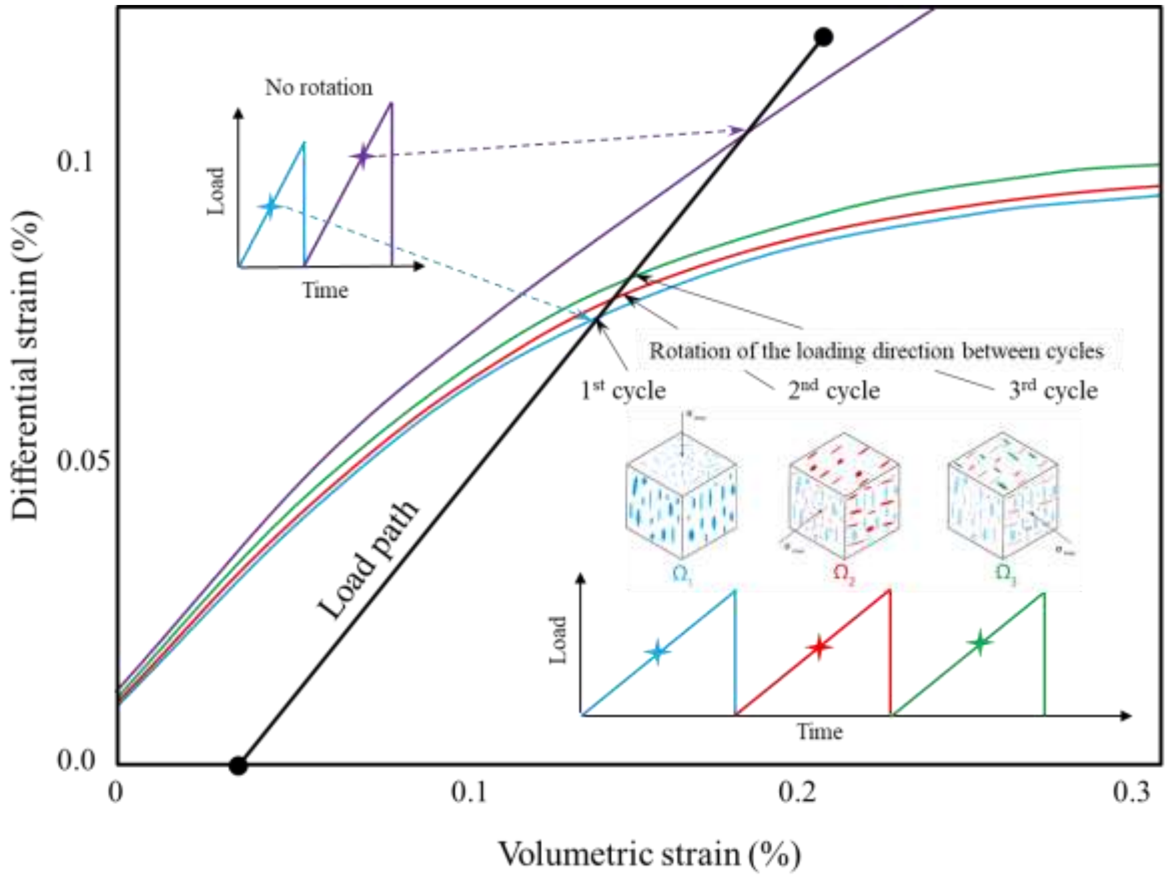

Fig. 4. Evolving yield envelope for loading cycles in which the maximum load is applied in the same direction cyclically and in which the maximum loading direction is sequentially rotated with respect to the sample.

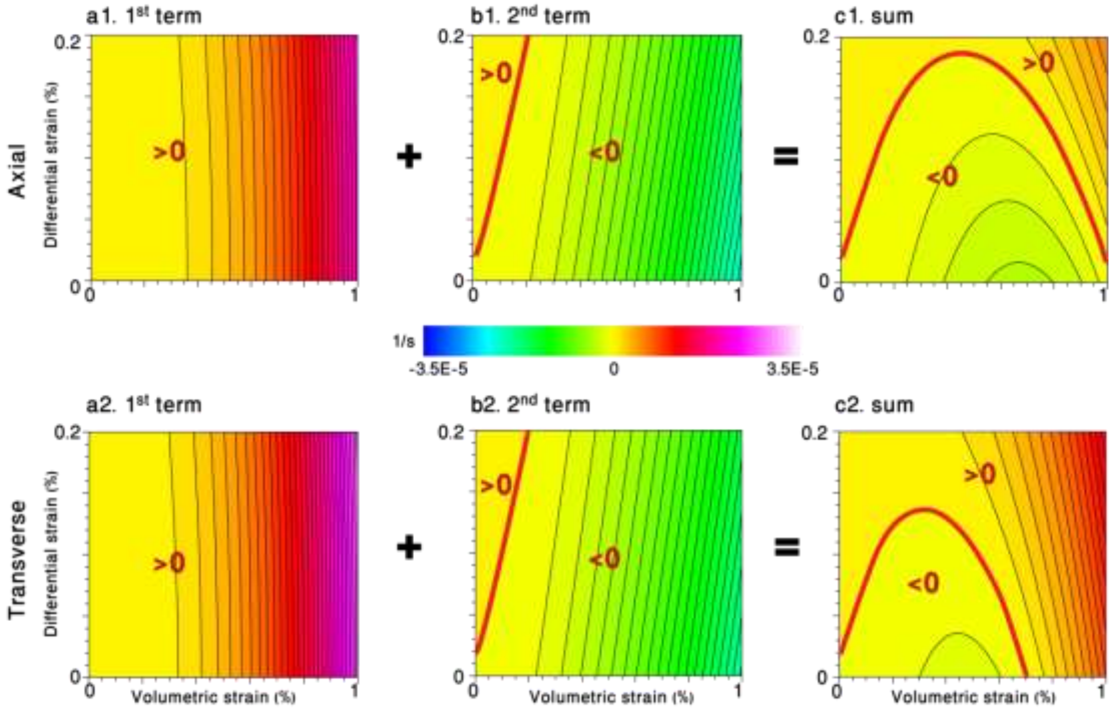

Fig. 5. Kinetics of the transverse damage components (Ω_1 , Ω_3) for initially anisotropic initial damage ($\Omega_1 < \Omega_2 = \Omega_3$). Upper raw represents the values for the larger (Ω_3) component and the lower raw for the smaller (Ω_1) component. The pattern for both components, 1st (a1, a2) and 2nd (b1, b2) terms are similar, but their different values lead~~s~~ to significantly different size of the yield envelope (c1, c2).

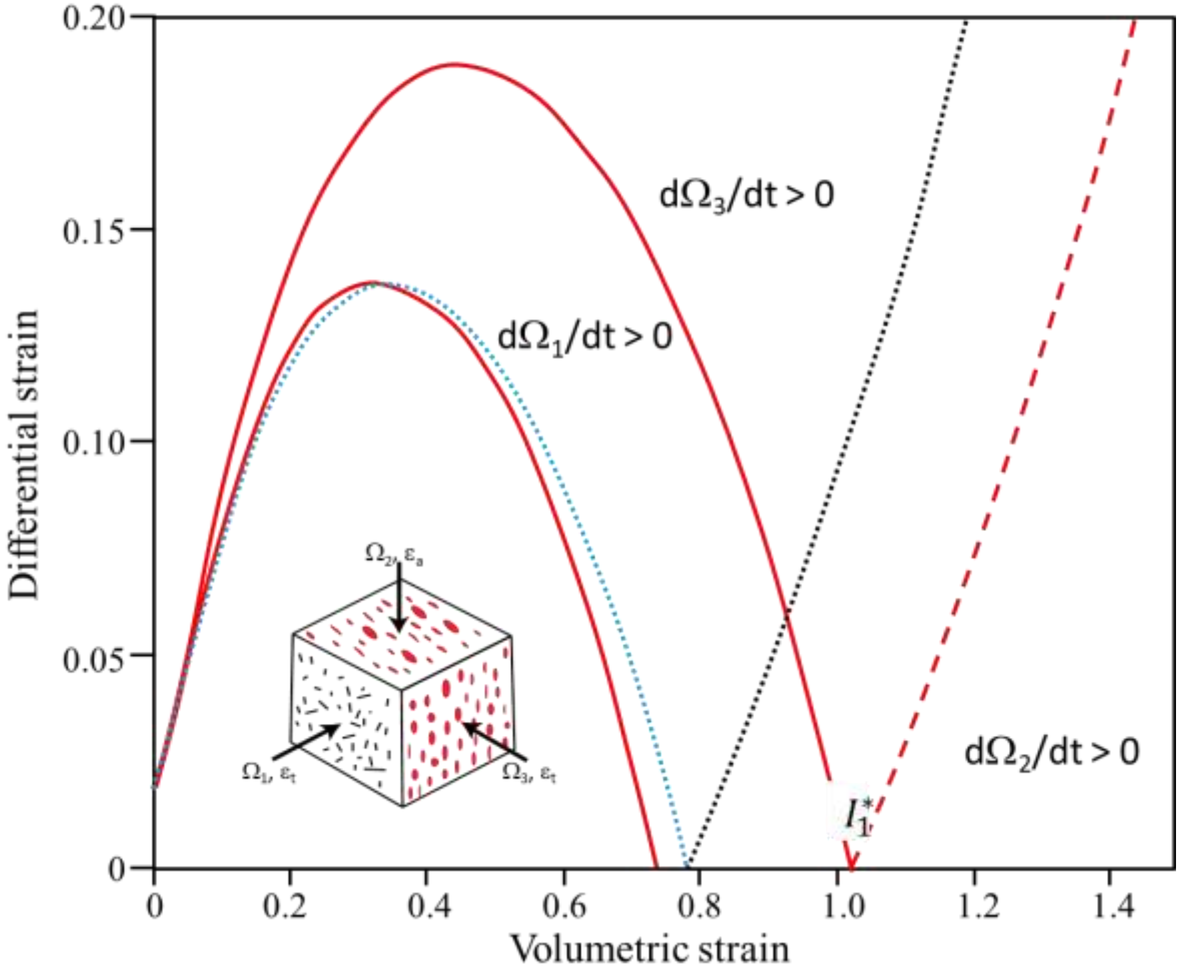

Fig. 6. Yield envelope for initially anisotropic material ($\Omega_1 < \Omega_2 = \Omega_3$). The envelope for the smallest transverse (Ω_1) component (red line) is almost the same as for the initially isotropic material (dotted blue line). The envelope for larger transversal component (Ω_3) is significantly larger than for the component Ω_1. The axial damage component (Ω_2) is accumulated only under high confining conditions.

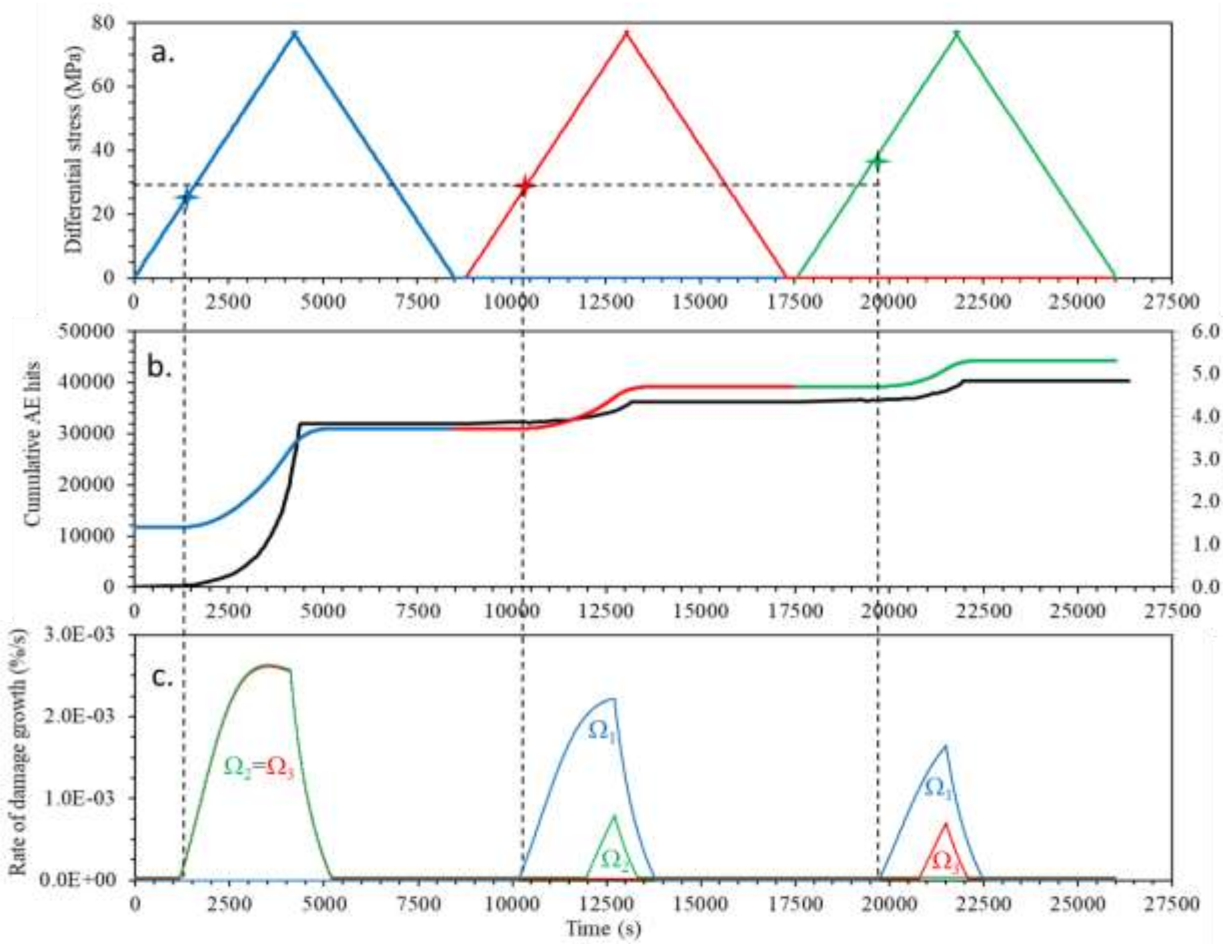

Fig. 7. Comparison between experimental results and modelling. (a) Sequential rotational conventional triaxial loading; markers show the onset of the observed AE (black line in (b)). Colored line in (b) shows the simulated damage accumulated during the loading. (c) rate of damage accumulation.

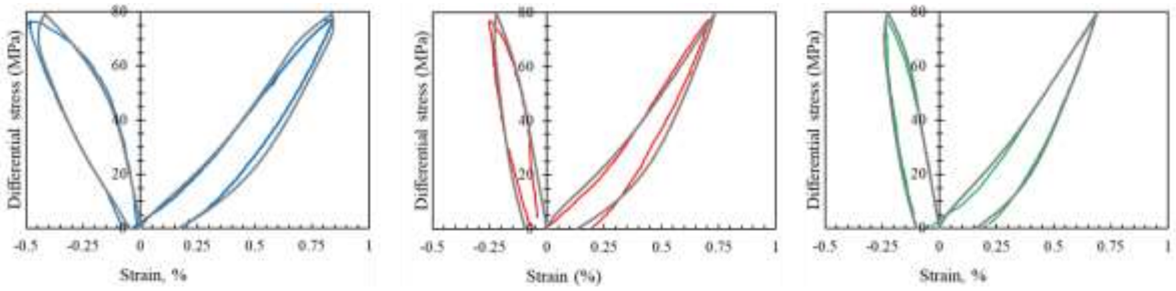

Fig. 8. Comparison between observed (colored lines) and simulated (grey lines) stress-strains for three loading cycles (blue, red, green).

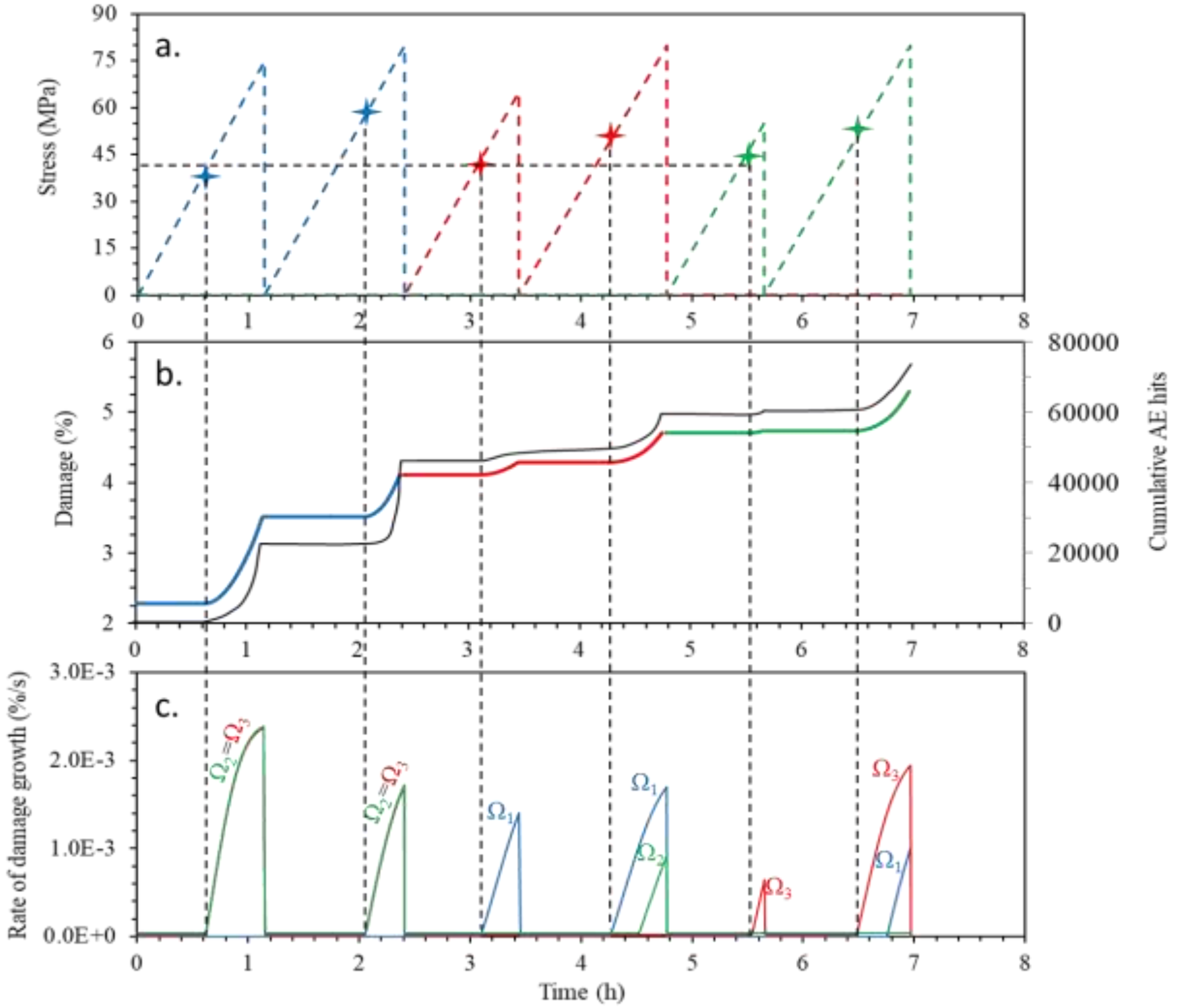

Fig. 9. Comparison between experimental results and modelling. (a) Cyclic sequential rotational conventional triaxial loading; the markers show the onset of the observed AE (black line in (b)). Colored line in (b) shows the simulated damage accumulated during the loading. (c) rate of damage accumulation.

Figure Captions

Figure 1. Three different deformational regimes and growing yield surface neglecting the cohesive force.

Figure 2. Damage kinetics for initially isotropic damage ($\Omega_1 = \Omega_2 = \Omega_3$) under conventional triaxial loading. (a) The 1st term is the same for all damage components. The 2nd term for axial component (b1) significantly differs from the values for the transversal components (b2). The damage kinetics in the axial direction (c1) differs from the transversal components(c2) which is similar in shape but not necessarily in values to the conventional scalar criterion.

Figure 3. Yield envelope for initially isotropic material.

Figure 4. Evolving yield envelope for loading cycles in which the maximum load is applied in the same direction cyclically and in which the maximum loading direction is sequentially rotated with respect to the sample

Figure 5. Kinetics of the transverse damage components (Ω_1 , Ω_3) for initially anisotropic initial damage ($\Omega_1 < \Omega_2 = \Omega_3$). Upper raw represents the values for the larger (Ω_3) component and the lower raw for the smaller (Ω_1) component. The pattern for both components, 1st (a1, a2) and 2nd (b1, b2) terms are similar, but their different values lead~~s~~ to significantly different size of the yield envelope (c1, c2).

Figure 6. Yield envelope for initially anisotropic material ($\Omega_1 < \Omega_2 = \Omega_3$). The envelope for the smallest transverse (Ω_1) component (red line) is almost the same as for the initially isotropic material (dotted blue line). The envelope for larger transversal component (Ω_3) is significantly larger than for the component Ω_1 . The axial damage component (Ω_2) is accumulated only under high confining conditions

Figure 7. Comparison between experimental results and modelling. (a) Sequential rotational conventional triaxial loading; markers show the onset of the observed AE (black line in (b)). Colored line in (b) shows the simulated damage accumulated during the loading. (c) rate of damage accumulation

Figure 8. Comparison between observed (colored lines) and simulated (grey lines) stress-strains for three loading cycles (blue, red, green).

Figure 9. Comparison between experimental results and modelling. (a) Cyclic sequential rotational conventional triaxial loading; the markers show the onset of the observed AE (black line in (b)). Colored line in (b) shows the simulated damage accumulated during the loading. (c) rate of damage accumulation.

Appendix A

Thermodynamic relations

The presented formulation is based on balance equation of the irreversible thermodynamics of the continuum media with internal variables (Malvern 1969, Coussy 1995). We consider the system with density of the free energy, *F*, to be a function of:

$$F = F(T, \varepsilon_{ij}, \Omega_{ij}, \psi_{ij}, \zeta) \tag{1}$$

where T – temperature, ε_{ij} – elastic strain tensor, ψ_{ij} – compaction tensor, Ω_{ij} – the damage tensor, and ζ is the change in volume fluid content defined by Biot (1941) (see also Detournay & Cheng 1993). Since each variable can vary independently of the other variables, Gibbs relation can be written as (Gibbs 1961):

$$dF = -SdT + \frac{\partial F}{\partial \varepsilon_{ij}} d\varepsilon_{ij} + \frac{\partial F}{\partial \Omega_{ij}} d\Omega_{ij} + \frac{\partial F}{\partial \psi_{ij}} d\psi_{ij} + \frac{\partial F}{\partial \zeta} d\zeta \tag{2}$$

where $S = -\frac{\partial F}{\partial T}$ is entropy density (Einstein's summation convention is assumed).

The balance equation for the density of the internal energy, U, includes three source terms associated with shear heating (stress, σ_{ij}, times strain rate or time derivative of the total strain rate tensor, e_{ij}), energy dissipation due to heat flux, Q_i, and the advective flux due to fluid flow (eq. 71 from Coussy *et al.* 1998):

$$\frac{dU}{dt} = \frac{d}{dt}(F + TS) = \sigma_{ij} e_{ij} - \nabla_i Q_i - \nabla_i\left[\left(h_f + Ts_f\right) q_i\right] \tag{3}$$

where q_i is fluid flux, h_f is the enthalpy or Gibbs potential of the fluid, which is a function of the fluid pressure, p_f, and temperature; s_f is the entropy of the fluid. Similarly, the entropy balance equation includes positive entropy production, Γ, divergence of the heat flux, and similar advective term due to fluid flow (eq. 72 from Coussy *et al.* 1998):

$$\frac{dS}{dt} = \frac{\Gamma}{T} - \nabla_i\left(\frac{Q_i}{T}\right) - \nabla_i\left(q_i\, s_f\right) \tag{4}$$

The stress tensor and the fluid pressure are defined as (Malvern 1969, Coussy 1995):

$$\sigma_{ij} = \frac{\partial F}{\partial \varepsilon_{ij}} \tag{5}$$

$$p_f = \frac{\partial F}{\partial \zeta} \tag{6}$$

Fluid mass conservation is:

$$\frac{d\zeta}{dt} = -\nabla_i(q_i) \tag{7}$$

Combining (2, 3, 4) and using (5, 6, 7) we get a final expression for the local entropy production in a form:

$$\Gamma = -\frac{Q_i}{T}\nabla_i T - q_i \nabla_i p_f + \sigma_{ij}\left(\mathrm{e}_{ij} - \frac{d\varepsilon_{ij}}{dt}\right) - \frac{\partial F}{\partial \Omega_{ij}}\frac{d\Omega_{ij}}{dt} - \frac{\partial F}{\partial \psi_{ij}}\frac{d\psi_{ij}}{dt} \tag{8}$$

First and second terms represent dissipation associated with heat transport and fluid flow. The Fourier and Darcy laws establish linear relations between temperature and fluid pressure gradients with corresponding fluxes:

$$Q_i = -K_{ij}^{T}\nabla_j T \tag{9a}$$

and

$$q_i = -K_{ij}^{F}\nabla_j p_f \tag{9b}$$

where K_{ij}^{T} and K_{ij}^{F} are positively defined thermal conductivity and permeability tensors.

The elastic strain tensor is the difference between total, g_{ij}, and irreversible compaction, ψ_{ij}, tensors:

$$\varepsilon_{ij} = g_{ij} - \psi_{ij} \tag{10}$$

Taking the time derivative of (10) and substituting the total strain rate tensor, $\mathrm{e}_{ij} = dg_{ij}/dt$, into (8), the part of the total dissipation, Γ_{DC}, associated with evolving damage and compaction (three last term of Eq. 8) is expressed as a sum of two terms proportional to the damage and compaction rates:

$$\Gamma_{DC} = -\frac{\partial F}{\partial \Omega_{ij}}\frac{d\Omega_{ij}}{dt} + \left(\sigma_{ij} - \frac{\partial F}{\partial \psi_{ij}}\right)\frac{d\psi_{ij}}{dt} > 0 \tag{11}$$

For small deviations from equilibrium, the entropy production or dissipation potential may be approximated as a quadratic function of the rate of the internal variables. In this case constitutive equations give the thermodynamic fluxes as a linear function of the thermodynamic forces (Malvern 1969, DeGroot & Mazur 2013) also known as the Onsager's (1931) relations:

$$\frac{d\psi_{ij}}{dt} = C_{ijnm}^{\psi\psi}\left(\sigma_{ij} - \frac{\partial F}{\partial \psi_{ij}}\right) - C_{ijnm}^{\psi\Omega}\frac{\partial F}{\partial \Omega_{ij}} \tag{12a}$$

$$\frac{d\Omega_{nm}}{dt} = C_{ijnm}^{\Omega\psi}\left(\sigma_{ij} - \frac{\partial F}{\partial \psi_{ij}}\right) - C_{ijnm}^{\Omega\Omega}\frac{\partial F}{\partial \Omega_{ij}} \tag{12b}$$

These phenomenological kinetic equations guarantee the non-negative entropy production if the cells of the matrix of the kinetic coefficients

$$C_{ijnm} = \begin{vmatrix} C_{ijnm}^{\psi\psi} & C_{ijnm}^{\psi\Omega} \\ C_{ijnm}^{\Omega\psi} & C_{ijnm}^{\Omega\Omega} \end{vmatrix} \tag{13}$$

meet several conditions (Malvern 1969, DeGroot & Mazur 2013). Matrixes of the diagonal cells ($C_{ijnm}^{\psi\psi}$, $C_{ijnm}^{\Omega\Omega}$) must be positively defined. Off-diagonal terms are usually taken to be either symmetric or antisymmetric. Following poroelastic damage model of Hamiel *et al.* (2004b) and Lyakhovsky *et al.* (2015) we adopt antisymmetric structure ($C_{ijnm}^{\Omega\psi} = -C_{ijnm}^{\psi\Omega}$) of the kinetic matrix (13). These conditions assure positive dissipation (11).

Further model formulation, demonstrating its main features as well as its calibration, verification, and application to specific problems require definition of the energy function (1) and kinetic coefficients (13). In the Appendix B we briefly discuss the isotropic, scalar formulation, which instead of the tensorial damage-compaction variables operates with the scalar damage, α, equal to the squared value, $\alpha = \Omega^2$, derived by Panteleev *et al.* (2021), and porosity, φ. Scalar Ω and φ variables are connected with the tensor variables as:

$$\Omega_{ij} = \Omega\,\delta_{ij} \tag{14a}$$

$$\psi_{ij} = \varphi\,\delta_{ij} \tag{14b}$$

The complete anisotropic formulation is presented in the Appendix C.

Appendix B

Scalar poroelastic damage model

Following Biot's theory of poroelasticity (Biot 1941, 1956) the free energy of a poro-elastic medium, *F*, is a sum of the elastic energy and the poroelastic coupling term of the saturated medium with the Biot modulus, *M*, and the Biot coefficient for porous media, β:

$$F = \frac{\lambda(\alpha,\varphi)}{2} I_1^2 + \mu(\alpha,\varphi) I_2 - \gamma(\alpha,\varphi) I_1 \sqrt{I_2} + \frac{1}{2} M[\beta I_1 - \zeta + \varphi]^2 + Ch\,\gamma_m\,\alpha \tag{15}$$

In the literature discussing Biot poroelasticity, this coefficient is often noted as α. To avoid a duplicate notation we use α for the scalar damage and change the notation for the Biot coefficient to β.

Since the target model is isotropic, the energy function may depend only on invariants of the elastic strain tensor, ε_{ij} ($I_1 = \varepsilon_{ii}$, $I_2 = \varepsilon_{ij}\varepsilon_{ij}$). Following (Hamiel, *et al.* 2004b, Lyakhovsky *et al.* 2015) the elastic energy for nonlinear damaged media includes two Hookean terms with the Lame drained moduli λ, μ, and an additional non-linear term with strain coupling modulus γ. Value of this additional modulus varies from zero for damage free material with $\alpha = 0$ to $\gamma = \gamma_m$ at material failure with $\alpha = 1$ (Lyakhovsky *et al.* 1997). Following Gajst (2020), we introduce the damage-dependent term with the non-dimensional coefficient *Ch*. Below we will show that this term allows accounting for the cohesive force which is important for loading conditions with low confining pressures.

Differentiation of the poroelastic energy (15) according to the constitutive relations (5, 6), the stress tensor, σ_{ij}, and fluid pressure, p_f, are:

$$\sigma_{ij} = \frac{\partial F}{\partial \varepsilon_{ij}} = \left(\lambda - \frac{\gamma}{\xi}\right) I_1 \delta_{ij} + (2\mu - \gamma\xi)\varepsilon_{ij} + \beta M(\beta I_1 - \zeta + \varphi) \tag{16}$$

$$p_f = \frac{\partial F}{\partial \zeta} = M(-\beta I_1 + \zeta - \varphi) \tag{17}$$

where $\xi = I_1/\sqrt{I_2}$ is the strain invariant ratio changing from $\xi = -\sqrt{3}$ for isotropic compaction to $\xi = \sqrt{3}$ for isotropic dilation. Using the assumption that $\lambda = Const.$ and both μ, γ linearly depend on the damage (Agnon & Lyakhovsky 1995), the derivatives of the energy function (15) are the effective stress:

$$\sigma_{ij} - \frac{\partial F}{\partial \varphi}\,\delta_{ij} = \sigma_{ij}^{eff} \tag{18}$$

and damage induced energy change:

$$\frac{\partial F}{\partial \alpha} = \gamma_m(-\,I_2\,(\xi - \xi_0) + Ch) \tag{19}$$

where ξ_0 is the critical value of the strain invariant ratio corresponding to the conditions of the Coulomb failure criteria (see Lyakhovsky *et al.* 1997 for details). Substituting the derivatives (18, 19) into kinetic equations (12) and accounting to the scalar nature of the damage, α, and porosity, φ, variables (14), and using the mean stress($\sigma_m = -\sigma_{kk}/3$), the coupled kinetic equations are reduced to (see Hamiel *et al.* 2004b, Lyakhovsky *et al.* 2015, and references therein):

$$\frac{d\varphi}{dt} = -A\,\sigma_m - D\,[I_2(\xi - \xi_0) - Ch] \tag{20}$$

$$\frac{d\alpha}{dt} = D\,\sigma_m + C_d[I_2(\xi - \xi_0) - Ch] \tag{21}$$

Hamiel et al. (2004b) suggested that the coupling coefficients *D* is a power-law expression of the effective pressure, $D \sim \sigma_m^N$. They demonstrated that the transition from positive to negative values of the slope of the yield curve (yield cap) is a general feature of the model. Here we modify the previous formulation using strain invariants

I_1, $\sqrt{I_2}$ and $\sigma_m = -K\,I_1$ (*K* is a bulk modulus); and also following Gajst *et al.* (2020) *D*-value exponentially decreases with damage:

$$D = C_d\ D_1 e^{-D_2\alpha}\,(-I_1)^N\sqrt{I_2}/K \tag{22}$$

$N>0$, D_1 and D_2 values define the shape of the yield envelope. The form (22) is defined only for compaction ($I_1 \leq 0$); D_1 is either constant or function of the porosity constrained using strain-defined yielding envelope. With this assumption, the kinetic for damage accumulation (21) is:

$$\frac{d\alpha}{dt} = C_d\left[D_1 e^{-D_2\alpha}(-I_1)^{N+1}\sqrt{I_2} + I_2(\xi - \xi_0) - Ch\right] \tag{23}$$

This form of the damage kinetic equation predicts the onset of damage accumulation ($\frac{d\alpha}{dt} = 0$) for the intact material ($\alpha = 0$), or the yield condition:

$$D_1(-I_1)^{N+1}\sqrt{I_2} + I_2(\xi - \xi_0) - Ch = 0 \tag{24}$$

Under shear load needed to overcome the cohesive force ($\tau_h = 2\mu_0\varepsilon_h$) with zero volumetric strain ($I_1 = 0,\ \xi = 0, \text{and}\ I_2 = 2\varepsilon_h^2$), the coefficient *Ch* is equal to:

$$Ch = -\xi_0\,\frac{\tau_h^2}{2\mu_0^2} \tag{25a}$$

Under large hydrostatic volumetric strains, neglecting the cohesive force, the onset of damage occurs at:

$$I_1^* = -\left(\frac{\sqrt{3}+\xi_0}{\sqrt{3}\cdot D_1}\right)^{1/N} \tag{25b}$$

The equations (25a, b) define two endmember yield values. The entire yield shape may be calculated for any given volumetric strain between zero and I_1^* by solving (24) as a quadratic equation for $\sqrt{I_2}$:

$$\sqrt{I_2} = \frac{D_1(-I_1)^N + I_1 + \sqrt{(D_1(-I_1)^N + I_1)^2 - 4\,\xi_0\,Ch}}{2\,\xi_0} \tag{25c}$$

The positive radical sign provides correct solution for $Ch = 0$. Figures B1-B3 show sensitivity of the shape and size of the yield envelope to the change of the model parameters D_1, *N*, and *Ch* values calculated using (25c). For N=1 and non-cohesive material (*Ch*=0) the envelope increases with decrease D_1 value keeping roughly self-similar shape (Fig. B1). Changing power index value *N* affects the shape of the envelope (Fig. B2). In these cases, D_1 values were rescaled to get the same volumetric strain $I_1^* = -3.5\%$ according to Eq. (25b). Non-zero *Ch* value for the cohesive material with N=1 and D_1=15 shifts envelope to larger differential strain values under low volumetric strains (Fig. B3). The shown set of surfaces for *Ch* =0–1.0 10^{-6}

corresponds to cohesive force values changing from zero to ~15 MPa for rock with shear modulus $\mu_0 = 10$ GPa. For typical cohesive force values of a few MPa, this model modification is important under relatively low confining pressures but may be neglected when confining pressures are higher (of the order of tens of MPa).

Appendix C

Anisotropic poroelastic damage model

The energy function of the anisotropic material with the damage tensor, Ω_{ij}, cannot be formulated only in terms of strain invariants I_1, I_2 of the elastic strain tensor, ε_{ij} ($I_1 = \varepsilon_{ii}$, $I_2 = \varepsilon_{ij}\varepsilon_{ij}$) used for the scalar model (eq. 15). Following Murti *et al.* (1991) and Zhang & Cai (2010) the energy function should also depend on the invariants of the tensor, $\varepsilon_{ij}^{(\Omega)}$, which is the symmetrized product of the elastic strain and damage tensors:

$$\varepsilon_{ij}^{(\Omega)} = \frac{1}{2}\left(\varepsilon_{ik}\Omega_{kj} + \varepsilon_{jk}\Omega_{ki}\right) \tag{26}$$

The invariants $I_1^{(\Omega)}$ and $I_2^{(\Omega)}$ of this tensor are:

$$\begin{gathered} I_1^{(\Omega)} = \varepsilon_{ik}\Omega_{kj}\delta_{ij} = \\ = \varepsilon_{11}\Omega_{11} + \varepsilon_{22}\Omega_{22} + \varepsilon_{33}\Omega_{33} + 2\varepsilon_{12}\Omega_{12} + 2\varepsilon_{23}\Omega_{23} + 2\varepsilon_{13}\Omega_{13} \end{gathered} \tag{27}$$

$$\begin{gathered} I_2^{(\Omega)} = \varepsilon_{ij}^{(\Omega)}\varepsilon_{ij}^{(\Omega)} = \\ = (\varepsilon_{11}\Omega_{11} + \varepsilon_{12}\Omega_{12} + \varepsilon_{13}\Omega_{13})^2 + \\ +(\varepsilon_{12}\Omega_{12} + \varepsilon_{22}\Omega_{22} + \varepsilon_{23}\Omega_{23})^2 + \\ +(\varepsilon_{13}\Omega_{13} + \varepsilon_{23}\Omega_{23} + \varepsilon_{33}\Omega_{33})^2 + \\ +\left(\varepsilon_{11}\Omega_{12} + \varepsilon_{22}\Omega_{12} + \varepsilon_{23}\Omega_{13} + \varepsilon_{13}\Omega_{23} + \varepsilon_{12}(\Omega_{11} + \Omega_{22})\right)^2 + \\ +\left(\varepsilon_{23}\Omega_{12} + \varepsilon_{11}\Omega_{13} + \varepsilon_{33}\Omega_{13} + \varepsilon_{12}\Omega_{23} + \varepsilon_{13}(\Omega_{11} + \Omega_{33})\right)^2 + \\ +\left(\varepsilon_{13}\Omega_{12} + \varepsilon_{12}\Omega_{13} + \varepsilon_{22}\Omega_{23} + \varepsilon_{33}\Omega_{23} + \varepsilon_{23}(\Omega_{22} + \Omega_{23})\right)^2 \end{gathered}$$

We extend energy function of the Panteleev *et al.* (2021) non-linear anisotropic damage rheology model by additional Biot terms similar to (15):

$$F = \left[\frac{\lambda_0}{2}I_1^2 + \mu_0 I_2\right] + \gamma\left[\xi_0 I_2^{(\Omega)} - I_1^{(\Omega)}\sqrt{I_2^{(\Omega)}}\right] + \frac{1}{2}M\left[\beta I_1 - \zeta + \psi_{ij}\delta_{ij}\right]^2 + Ch\,\frac{\gamma}{2}\,\Omega_{ij}\Omega_{ij} \tag{28}$$

The definitions (26-28) mean that the energy is the second order function of both elastic strain and damage tensors. Substituting energy function (28) into (5) and (6) the stress tensor is expressed as:

$$\sigma_{ij} = \frac{\partial F}{\partial \varepsilon_{ij}} = \lambda_0 I_1 \delta_{ij} + 2\mu_0 \varepsilon_{ij} - \gamma \frac{\partial I_1^{(\Omega)}}{\partial \varepsilon_{ij}} \sqrt{I_2^{(\Omega)}} + \gamma \left(\xi_0 - \frac{I_1^{(\Omega)}}{2\sqrt{I_2^{(\Omega)}}} \right) \frac{\partial I_2^{(\Omega)}}{\partial \varepsilon_{ij}} +$$

$$+\beta M\,(\beta I_1 - \zeta + \psi_{kn}\delta_{kn})\delta_{ij} \qquad (29)$$

where

$$\frac{\partial I_1^{(\Omega)}}{\partial \varepsilon_{lm}} = \Omega_{lm},$$

$$\frac{\partial I_2^{(\Omega)}}{\partial \varepsilon_{lm}} = \frac{1}{2}(\Omega_{li}\varepsilon_{ik}\Omega_{km} + \Omega_{mi}\varepsilon_{ik}\Omega_{kl}) + \frac{1}{2}\left(\Omega_{lj}\varepsilon_{mk}\Omega_{kj} + \Omega_{mj}\varepsilon_{lk}\Omega_{kj}\right).$$

The fluid pressure is almost identical to (17)

$$p_f = \frac{\partial F}{\partial \zeta} = M\,(-\beta I_1 + \zeta - \psi_{kn}\delta_{kn}) \qquad (30)$$

Similar~~ly~~ to (18) the effective stress is defined as:

$$\sigma_{ij} - \frac{\partial F}{\partial \psi_{ij}} = \sigma_{ij}^{eff} \qquad (31)$$

In order to evaluate the energy dissipation and write the couples damage-compaction kinetic relations (12), the damage induced energy change should be calculated:

$$\frac{\partial F}{\partial \Omega_{ij}} = \gamma \left[\left(\xi_0 - \frac{I_1^{(\Omega)}}{2\sqrt{I_2^{(\Omega)}}} \right) \frac{\partial I_2^{(\Omega)}}{\partial \Omega_{ij}} - \varepsilon_{ij}\sqrt{I_2^{(\Omega)}} + Ch\,\Omega_{ij} \right] \qquad (32)$$

Formulating the tensor kinetic coefficients, we keep in mind that the coupling kinetic coefficient $D_{ijkn} = C_{ijnm}^{\Omega\psi}$ of eq. (13) should decrease with damage accumulation and expect that this will allow reproducing the directional Kaizer Effect observed under true triaxial loading (Browning *et al.* 2018). Similarly to the exponential relation (22), we suggest that the matrix D_{ijkn} of the kinetic coefficients exponentially decrease with damage accumulation. Extending this idea to the complete tensor form and using the same dependency of the coupling term as in the scalar model (22), we suggest the following form of the coupling kinetic coefficient D_{ijkn}:

$$D_{ijkn} = D_1 exp\left[-D_2\Omega_{ij}\right]\delta_{kn}\,(-I_1)^N\sqrt{I_2} \qquad (33)$$

where we use the standard definition of the exponent of the tensor $\boldsymbol{X}$ by means of its series representation (Hirsch *et al.* 1974)

$$exp(\boldsymbol{X}) = \sum_{m=0}^{\infty} \frac{\boldsymbol{X}^m}{m!} \qquad (34)$$

Note that the principal values of the tensor $exp(\boldsymbol{X})$ are equal to the $exp(X_k)$.

The most conservative assumption to define the components of the matrix $C_{ijnm}^{\Omega\Omega}$ in (13) is the absence of the interaction between different components, i.e., $C_{ijnm}^{\Omega\Omega} = L\left(\delta_{ik}\,\delta_{jn} + \delta_{in}\,\delta_{jk}\right)$, and L is proportional to $1/\sqrt{\Omega_{ij}\Omega_{ij}}$ as it was suggested by verified by Panteleev *et al.* (2021) using results of true-triaxial rock mechanics experiments ignoring effects of compaction. With these kinetic coefficients, the equation (12b) for the damage evolution has the same structure as the damage kinetic equation (23) of the scalar model.

$$\frac{d\Omega_{ij}}{dt} = D_1 exp\left[-D_2\Omega_{ij}\right]\,(-I_1)^N\sqrt{I_2}\,\sigma_m^{eff} +$$

$$+\frac{L}{\sqrt{\Omega_{kn}\Omega_{kn}}}\left[\varepsilon_{ij}\sqrt{I_2^{(\Omega)}} + \left(\frac{I_1^{(\Omega)}}{2\sqrt{I_2^{(\Omega)}}} - \xi_0\right)\frac{\partial I_2^{(\Omega)}}{\partial\Omega_{ij}} - Ch\,\Omega_{ij}\right] \qquad (35)$$

The equation for the evolving compaction (12a) includes two terms. The first term, equal to $C_{ijnm}^{\psi\psi}\sigma_{nm}^{eff}$ describe compaction/extension with the rate proportional to the effective stress. The second one is the damage-related coupling term, which is the $\frac{\partial F}{\partial\Omega_{ij}}$ multiplied to D_{ijkn}, and describes the compaction or dilation induced by the damage growth. Representing the effective stress as a superposition of the volumetric (P_e) and deviatoric (τ_{ij}) components allows to describe different mechanisms of the irreversible strain accumulation or ψ_{ij} kinetics. The pressure driven compaction under hydrostatic load is described by a well-known porosity reduction to its pressure-dependent equilibrium value or Athy's (1930) law. Lyakhovsky *et al.* (2021) modified the scalar Athy relation accounting not only for volumetric effects, but also directional effects associated with changes of the shape of pore space and accumulation of irreversible deviatoric strain components. The suggested 3-D equilibrium compaction strain, $\psi_{ij}^{(eq)}$, depends on both pressure and deviatoric stress components:

$$\psi_{ij}^{(eq)} = B_0\left[\delta_{ij} - exp\left(-\frac{\sigma_m^{eff}}{B_1}\delta_{ij} - \frac{\tau_{ij}}{B_2}\right)\right] \qquad (36)$$

and suggested kinetics of the pressure-driven 3-D compaction in the form

$$\frac{d\psi_{ij}}{dt} = A\left(\psi_{ij}^{(eq)} - \psi_{ij}\right)\sigma_m^{eff} \tag{37}$$

Neglecting the term with deviatoric stress or taking $B_2 \to \infty$ in (36) reduces both equilibrium compaction (36) and kinetic equation (37) to the traditional scalar Athy's (1930) law formulated in terms of material porosity.

Experimental studies suggest that permanent inelastic deformation is accumulated in high porosity rocks, but also is related to the damage accumulation. It starts accumulating with the onset of the acoustic emission and increases all the way up to brittle failure (e.g., Lockner 1993, 1998, Martin & Chandler 1994). This process is usually associated with the growth of microcracks and frictional sliding between grains, rather than closure of voids or open space between grans. For similar reasons, Hamiel *et al.* (2004a) related the rate of irreversible strain accumulation with the rate of their scalar damage growth. Keeping in mind that the scalar damage variable is equivalent to the squared damage tensor, we extend their relation to the tensor form keeping the same structure of functional relations:

$$\frac{d}{dt}\varepsilon_{ij}^{(ir)} = \begin{cases} C_V \dfrac{d(\Omega_{in}\Omega_{jm})}{dt}\tau_{nm}, & \dfrac{d(\Omega_{in}\Omega_{jm})}{dt} > 0 \\ 0, & \dfrac{d(\Omega_{in}\Omega_{jm})}{dt} \leq 0 \end{cases} \tag{38}$$

Here we combine both mechanisms and represent the static value of the tensor $\psi_{ij}^{(S)}$ as a sum of

$$\psi_{ij}^{(S)} = \psi_{ij}^{(eq)} + \varepsilon_{ij}^{(ir)} \tag{39}$$

The ~~Final~~ final kinetic equation (12a) for the ψ_{ij} tensor incorporates all the discussed mechanisms (to avoid very length equation D_{ijkn} and $\frac{\partial F}{\partial \Omega_{kn}}$ are not substituted here):

$$\frac{d\psi_{ij}}{dt} = A\left(\psi_{ij}^{(eq)} - \psi_{ij}\right)\sigma_m^{eff} + C_V \frac{d(\Omega_{in}\Omega_{jm})}{dt}\tau_{nm} - D_{ijkn}\frac{\partial F}{\partial \Omega_{kn}} \tag{40}$$

The kinetic equation for damage (35) and compaction (40) provide the close system of equations defining the 3-D evolution of the material properties. To study some basic model properties, we follow the assumption of Panteleev *et al.* (2021) that the principal directions of the damage tensor match the orientation of the principal loading axes. This assumption is supported by results of true-triaxial experiments (Browning *et al.* 2017, 2018) demonstrating orientation of distributed micro-cracks in the sample volume under limited load, well before their localization into narrow fault zones. Adopting the above assumptions, we re-write the stress-strain and damage kinetic relations for principal values in *k*-direction (no summation):

$$\sigma_k = \lambda_0 \, I_1 + 2\mu_0 \varepsilon_k + 2\mu_1 \Omega_k^2 \varepsilon_k - \gamma \Omega_k \sqrt{I_2^{(\Omega)}} - \gamma \xi^{(\Omega)} \Omega_k^2 \varepsilon_k + \beta \, p_f \tag{41}$$

and

$$\frac{d\Omega_k}{dt} = D_1 exp[-D_2 \Omega_k] \, (-I_1)^N \sqrt{I_2} \, \sigma_m^{eff} + \frac{L}{\sqrt{\Omega_l \Omega_l}} \left[\varepsilon_k \sqrt{I_2^{(\Omega)}} + \left(\frac{I_1^{(\Omega)}}{\sqrt{I_2^{(\Omega)}}} - 2\xi_0 \right) \varepsilon_k^2 \Omega_k - Ch \, \Omega_k \right] \tag{42}$$

We note that for the isotropic damage ($\Omega_1 = \Omega_2 = \Omega_3$) summation of free damage rate components give~~s~~ the same equation as for the scalar damage with the same damage-dependent yield envelope.

$$\frac{d\psi_k}{dt} = A \left(\psi_k^{(eq)} - \psi_k \right) \sigma_m^{eff} + C_V \frac{d(\Omega_k^2)}{dt} \tau_k + \\ + D_1 exp[-D_2 \Omega_k] \, (-I_1)^N \sqrt{I_2} \left[\varepsilon_k \sqrt{I_2^{(\Omega)}} + \left(\frac{I_1^{(\Omega)}}{\sqrt{I_2^{(\Omega)}}} - 2\xi_0 \right) \varepsilon_k^2 \Omega_k - Ch \, \Omega_k \right] \tag{43}$$

The first term of eq. (43) represents the compaction prior to the onset of the damage accumulation, which is 3-D extension of the scalar Athy's law compaction. According to this term the compaction approaches to its stress-dependent equilibrium value with the rate proportional to the effective pressure. The second term is 3-D equivalent to the damage-dependent irreversible strain accumulation with inverse of the effective viscosity or fluidity proportional to the rate of the damage accumulation. This term describes extension or compaction depending on the sign of the deviatoric stress component. The last term represents the coupling between damage and porosity kinetics. Its sign, extension or compaction, is defined by the expression in the square brackets and depends on the loading and damage values.

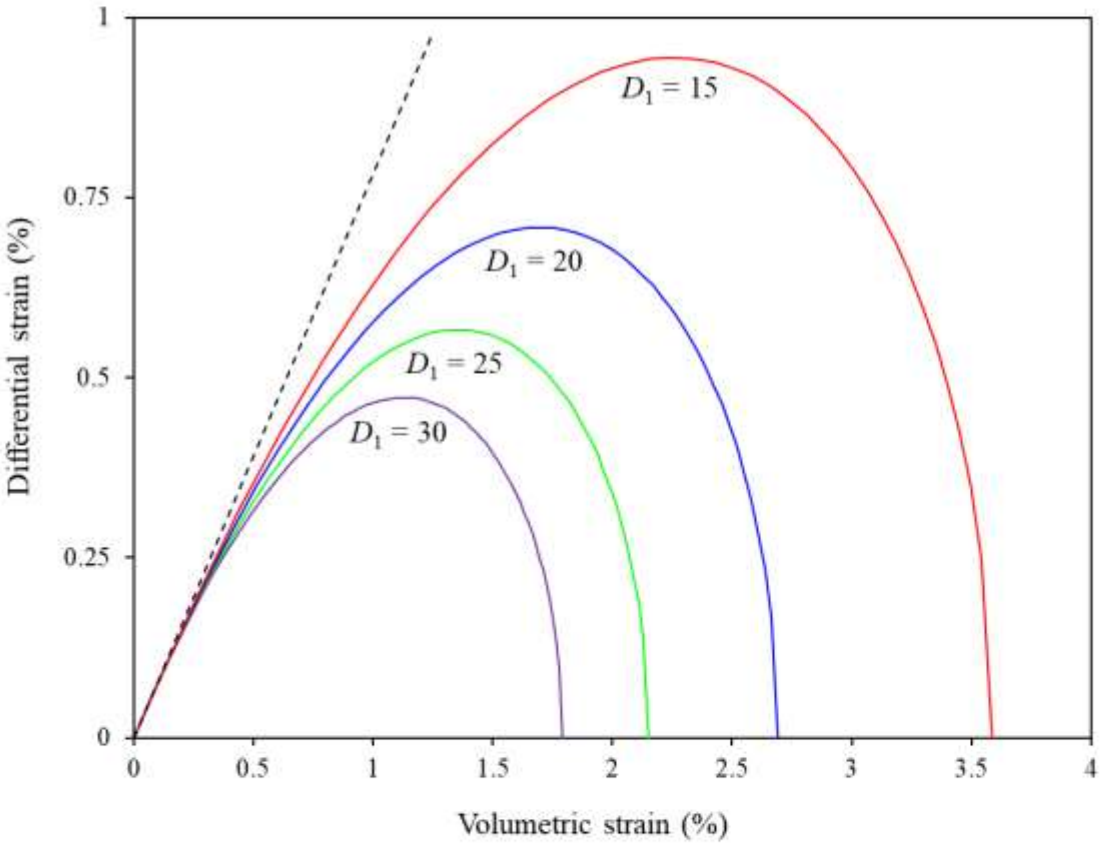

Fig. B1. Yield envelope size increase with decrease in *D*-value (*N*=1)

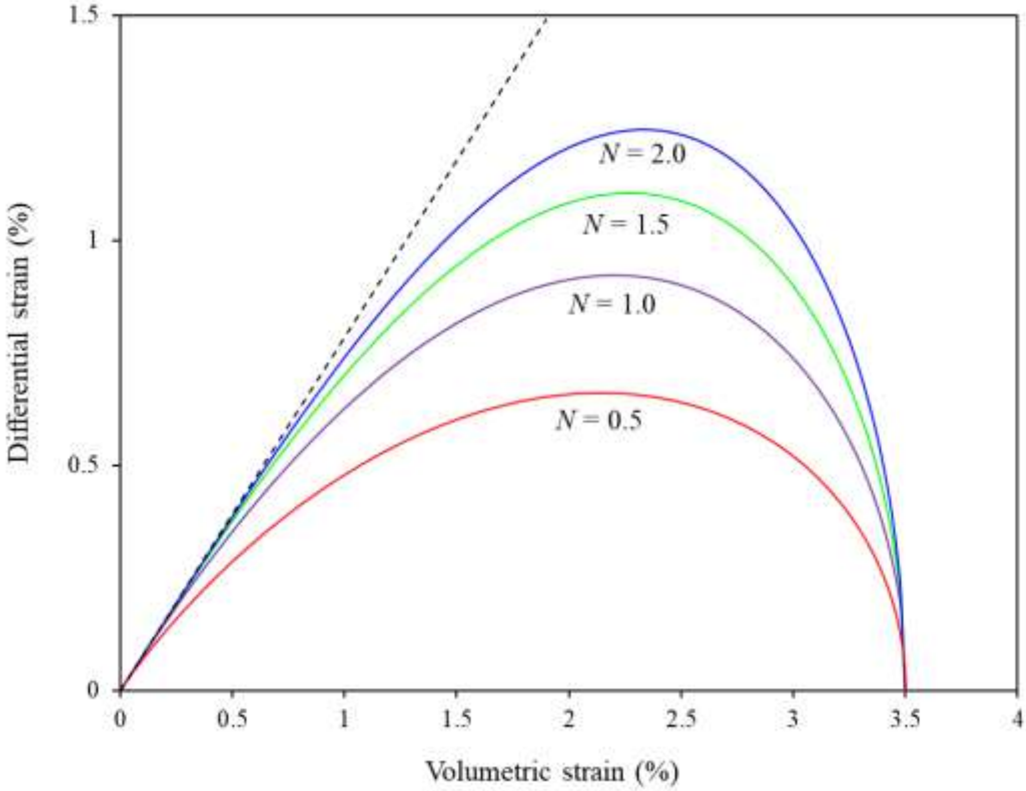

Fig. B2. Shape of the yield envelope for *N*-values changing between 0.5 and 2.0

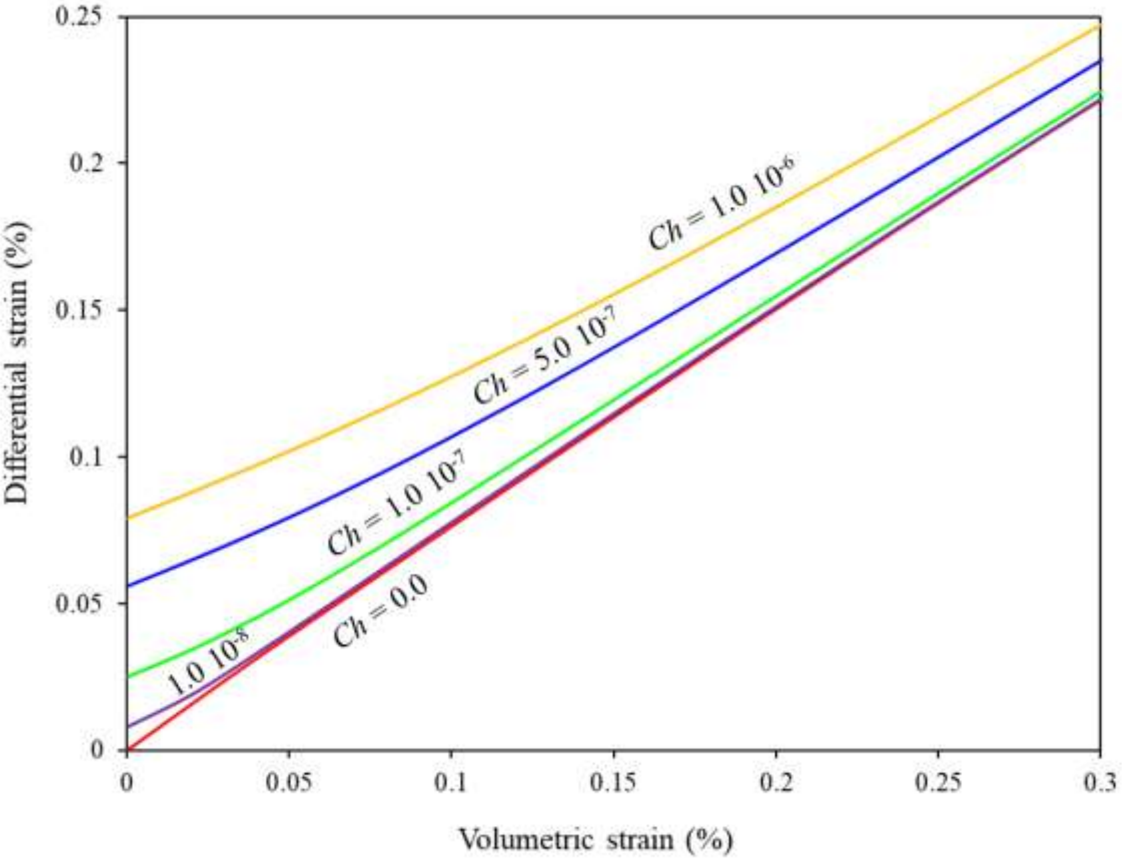

Fig. B3. The yield envelope is shifted up to higher differential strain values with increased *Ch* value (*N*=1 and *D*=15).

Figure Captions (Appendix B)

Figure B1. Yield envelope size increase with decrease in *D*-value (*N*=1)

Figure B2. Shape of the yield envelope for *N*-values changing between 0.5 and 2.0

Figure B3. The yield envelope is shifted up to higher differential strain values with increased *Ch* value (*N*=1 and *D*=15)